Correlation of Impact Conditions, Interface Reactions, Microstructural Evolution, and Mechanical Properties in Kinetic Spraying of Metals: A Review

Jaeick Kim and Changhee Lee

(Submitted April 3, 2016; in revised form July 26, 2016)

In the past, most studies into kinetic spraying technology focused on basic research, but a large portion of current research is devoted to industrial applications of the technology. To advance, however, studies about industrial applications of kinetic spraying require profound understanding of the scientific foundations of the kinetic spray process. Nevertheless, no one has yet provided a well-organized summary of the correlations among impact conditions, interface reactions, microstructural evolution, and mechanical properties across the whole field of kinetic spraying technology. This paper provides such an overview of these correlations for kinetic spraying of metals. For each correlation, the interactions between the given conditions and the material properties of the metal feedstock powder are the most influential. These interactions are so complicated that it is difficult to systematically classify all cases into certain types. Nonetheless, we try to explain and summarize the critical factors and their roles in each relationship.

1. Introduction

Kinetic spraying, or the cold gas dynamic spray process, is a method for deposition of micron-sized powder onto a target by accelerating particles to supersonic speeds (300–1200 m/s) using high-pressure gas with a convergent–divergent de Laval nozzle (Ref 1-8). Since the feedstock powder is deposited primarily through the kinetic energy of the supersonic acceleration without melting, coating layers with specific properties that provide various advantages over the thermal spray process can be produced (Ref 3, 9-18). Also, intimate bonding between the impact pairs can be induced through the creation of adiabatic shear instability at interface regions (Ref 19-23). Therefore, kinetic spraying technology has received much

attention for use in various industrial fields (i.e., automotive, aviation, defense, and energy) (Ref 24-27).

Research on kinetic spraying has been conducted since the 1990s. In the early days, most studies focused on determining the deposition mechanism of metals (Ref 19-23, 28-42). It was revealed that the creation of adiabatic shear instability at the periphery of the interface region played a dominant role in bond formation via severe plastic deformation (Ref 19-23, 28, 29). On this basis, the minimum particle velocity required for successful deposition was defined as the *critical velocity* of kinetic spraying, resulting from competition between the bonding (plastic deformation) and debonding (elastic recovery) energies (Ref 19). Early research defined the *rebound velocity* as the velocity at which successful deposition becomes impossible due to excessive elastic recovery (Ref 20, 36). Subsequently, the effects of process and powder conditions (impact conditions) on the deposition and interface behavior at the moment of impact were investigated (Ref 43-70). The factors related to particle velocity were found to be the most influential, although other factors, such as the relative hardness of the impact pairs, the particle/substrate temperature, the degree of oxidation, and the impact angle were also found to be important. Additionally, the characteristic microstructural evolution in kinetic-sprayed coating layers was elucidated, particularly for the interface region of the deposit (Ref 71-102). In many cases, refined structure was observed along the bonding interface, which seemed to be formed by grain refinement and static/dynamic restoration (Ref 74, 77-84). Nanoscale phase transformation or formation of intermetallic compounds appeared in local parts of the interface region (Ref 85-87). Various researchers also investigated the

Jaeick Kim and **Changhee Lee**, Kinetic Spray Coating Lab, Division of Materials Science and Engineering, Hanyang University, Seoul 133-791, South Korea. Contact e-mail: chlee@hanyang.ac.kr.

properties of kinetic-sprayed metal deposits (Ref 14, 16, 103-141). Specifically, some studies reported that the nanoscale mechanical properties of the interface region were superior to those of bulk metals (Ref 111, 112, 114). Of course, at the microscale, enhanced bond strength/density/hardness and high-density coating layers of metals were achieved without phase transformation or oxidation. However, the overall physical and chemical properties of a kinetic-sprayed coating layer cannot exceed the properties of bulk metals because of microdefects such as pores, cracks, and unbonded interface (Ref 12).

Thus, until recently, most research focused on fundamental investigation of kinetic spraying technology, but a large portion of current research is devoted to industrial applications of the technology. Diverse industrial fields are interested in kinetic spraying, and there is even applicability of the technology as a method for three-dimensional (3D) forming (additive manufacturing) (Ref 142-146). However, industrial applications of kinetic spraying require profound understanding of the physical foundations of the process. When such understanding is achieved, the requirements of many industrial fields could be satisfied and a database of various materials and conditions systematically prepared. Nevertheless, no one has yet provided a well-organized summary of the correlations among impact conditions, interface reactions, microstructural evolution, and mechanical properties across the whole field of kinetic spraying technology.

This paper provides such an overview of these correlations for kinetic spraying of metals, discussing each relationship sequentially in detail. The overall discussion focuses on understanding the critical factors and their roles in each relationship.

2. Effect of Impact Conditions on Interface Reactions

2.1 Outline

Many factors can be considered as impact conditions, but it is unnecessary to examine them one by one. For the kinetic spray process, the most influential impact conditions for interface reactions are particle velocity, the particle and substrate temperatures, the relative hardness of the particles and substrate, the oxidation state, and the impact angle.

2.2 Particle Velocity

Generally, in a kinetic spray process, feedstock material can be deposited on a target when the particle velocity is greater than the critical velocity. However, if particles are excessively accelerated, above the rebound velocity, the impacting particles rebound and successful deposition cannot be achieved. Thus, the interface reactions vary greatly according to the velocity of the particles in flight. The critical and rebound velocities result from the competition between the plastic deformation energy and the recoverable elastic energy. As is well known, the plastic

deformation of the impact pair is the dominant factor contributing to bonding in the kinetic spray process, whereas the recoverable elastic force is the major hindrance to bonding. The variation of the plastic deformation and recoverable elastic energies with particle velocity is shown in Fig. 1 (Ref 36). In the first stage of this plot, the plastic deformation energy (E_P) is smaller than the recoverable elastic energy (E_R), but the rate of increase of E_P is greater than that of E_R. However, at a certain point (the critical velocity), the situation reverses. This situation of greater E_P than E_R is not maintained continuously, because the rate of increase of E_P falls below that of E_R above the critical velocity. Thus, the rebound velocity is the point at which the predominance between E_P and E_R is re-reversed ($E_P \leq E_R$). In other words, since the critical and rebound velocity are the primary turning points in terms of deposition behavior, the interface reactions at the moment of impact can be classified into three cases: (1) below critical velocity, (2) between critical velocity and rebound velocity, and (3) above rebound velocity.

In case I, an insufficient amount of impact energy is provided by the particles. The degree of plastic deformation does not induce sufficient thermal energy for satisfactory interfacial bonding. As a result, the particles bounce off due to the recoverable elastic force stored in the particles and substrate. In terms of energy, this phenomenon occurs because the plastic deformation energy (bonding E) is smaller than the recoverable elastic energy (debonding E). In this case, the effects of strain and strain-rate hardening are more dominant than those of thermal softening, and adiabatic shear instability does not occur. Thus, there is no jetting (Ref 19) of the interface edge region and no sudden increase of strain or temperature [no thermal boost-up zone (Ref 21)].

In case II, the particles are traveling fast enough to produce sufficient impact energy. A significant amount of plastic deformation, with consequent thermal energy, is
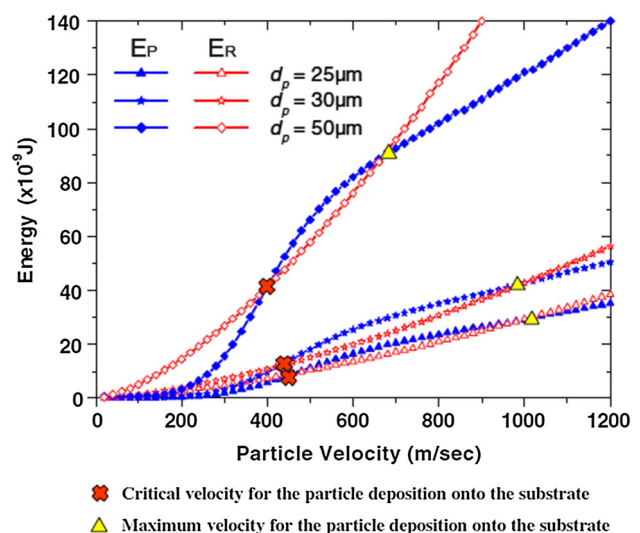

Fig. 1 Calculated plastic deformation (bonding) and recoverable elastic (debonding) energies for various sized Al–Si particles impacting onto a mild-steel substrate (Ref 36)

induced at the impact interface. Even though the shape-restoring phenomenon via the stored recoverable elastic energy at the interface region continues to occur in common with case I, the particles do not bounce off due to their intimate bonding with the substrate or other particles. In other words, in case II, the plastic deformation energy (bonding E) is greater than the recoverable elastic energy (debonding E). The thermal softening effect outweighs the strain and strain-rate hardening, and adiabatic shear instability is generated at the periphery of the interface region. Here, jetting occurs at the interface edge, with rapid increases in strain and temperature (occurrence of thermal boost-up zone).

In case III, plastic deformation of the impact pair is adequately induced by the impact of the rapidly accelerated particles. However, although the interfacial bond is well generated instantly, the bonded particles cannot withstand the subsequent rebound phenomenon caused by the excessive accumulated recoverable elastic energy in the impact pair. In case III, the amount of recoverable elastic energy converted from the impact energy is greater than the plastic deformation energy. This implies that the plastic deformation E (bonding E) again becomes smaller than the recoverable elastic energy (debonding E). The jetting and strain/temperature increase induced by the adiabatic shear instability can be observed at the interface region, but successful deposition cannot be achieved.

2.3 Particle and Substrate Temperatures

To obtain a proper interface reaction for successful deposition, use of a particle velocity faster than the critical velocity is the most important requirement in kinetic spraying. To induce an interface reaction similar to that of case II but at a relatively slow particle velocity, the critical velocity of the chosen feedstock powder can be lowered by enhancing the plastic deformability of the feedstock powder and substrate. Doing so generates an appropriate interface reaction for successful deposition. Figure 2 shows the effect of powder preheating on the deposition
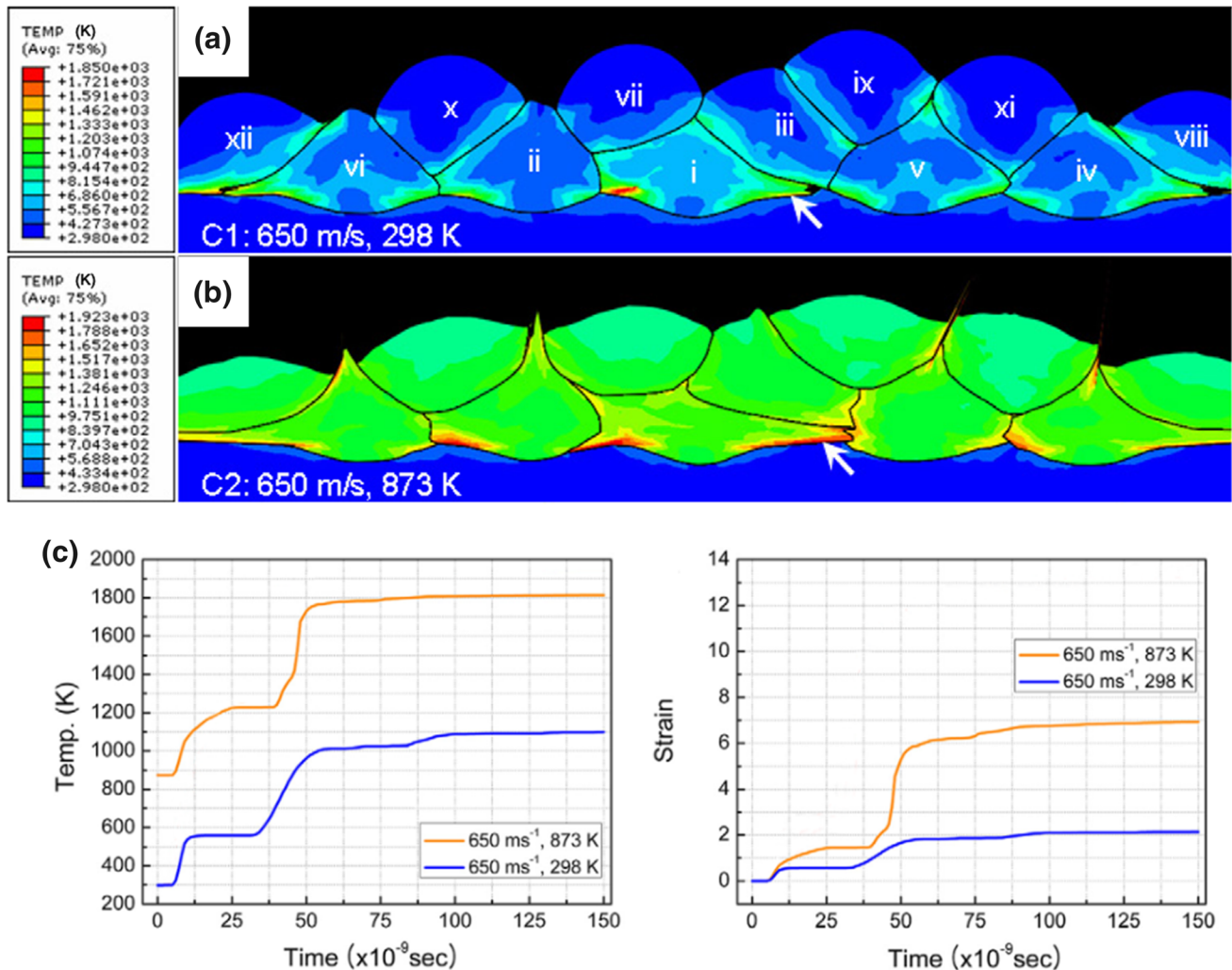

Fig. 2 Temperature distribution resulting from a multiparticle impact simulation of pure Ti at 600 °C and 2.5 MPa using N_2 gas (a) without preheating and (b) with preheating, and (c) the temperature and strain alteration vs. time for (a) and (b) (Ref 22)

behavior of pure Ti in kinetic spray deposition (Ref 22). As shown in Fig. 2(a), without preheating of the feedstock powder, the degree of particle plastic deformation was generally insignificant and no jetting occurred at the edge of the interface regions. In contrast, when the feedstock powder was preheated (Fig. 2b), the particles were severely plastic-deformed and some particles showed the jetting phenomenon. The temperature increase at the interface region became remarkable following preheating of the feedstock powder (Fig. 2c). In addition, the strain in the vicinity of the particle interface region was greatly enhanced by preheating the feedstock powder. This indicates that preheating of the feedstock powder can be helpful to minimize the critical velocity of a given material.

2.4 Relative Hardness of Particles and Substrate

Even for the same impact energy and identical feedstock powder, the interface reaction will vary depending on the target material. Figure 3 shows four kinds of impact behavior classified according to the relative hardness of the particles and substrate: soft–soft, hard–hard, soft–hard, and hard–soft (Ref 21). Naturally, the degree of plastic deformation is the same for similar pairs (soft–soft and hard–hard) (Fig. 3a, b), but it is biased toward the soft side for dissimilar pairs (soft–hard and hard–soft) (Fig. 3c, d). Thus, the division of impact energy consumption varies between similar and dissimilar pairs. For similar pairs, the impact energy is almost evenly consumed by the impacting and impacted parts, so it is somewhat difficult to heat either side of the interface to the melting point (comparatively high critical velocity). On the other hand, for dissimilar pairs, the impact energy is primarily consumed by the soft part, which is therefore more easily heated to the melting point (relatively low critical velocity). Practically, according to Bae et al. (Ref 21), the critical velocity of Al on Al (~750 m/s, soft–soft case) and Ti on Ti (~850 m/s, hard–hard case) is higher than that of Al on mild steel (~350 m/s, soft–hard case) or Ti on Al (~650 m/s, hard–soft case).

These four cases also differ with respect to high-temperature areas and aspects of energy development (Ref 21). As shown in Fig. 4(a) and (d), the soft–soft and hard–soft cases show the widest high-temperature areas, which means the widest chemical/metallurgical bonding area assisted by thermal energy. In both cases, the bonding (plastic deformation) energy is more dominant than the debonding (recoverable elastic) energy. It is obvious that the coating quality of these cases is usually excellent, as long as proper impact conditions are used. On the other hand, for the soft–hard case, the high-temperature area is only wide on the soft side (Fig. 4c). The bonding energy is not much higher than the debonding energy, unlike the soft–soft and hard–soft cases. Thus, the bonding quality is inferior to that of the prior cases in most situations. The hard–hard pair has the narrowest high-temperature area among the four pairs. Also, the bonding energy is lower than the debonding energy, regardless of particle velocity (Fig. 4d). Hence, successful deposition with high bonding quality is difficult to achieve for the hard–hard case.

2.5 Oxidation State

To obtain successful bonding in the kinetic spray process, the amount of thermal energy converted from plastic deformation at the moment of impact should be higher than a certain threshold. If the impact energy is consumed unnecessarily, particle–particle and particle–substrate bonding cannot be achieved. Unnecessary use of impact energy in kinetic spraying occurs primarily in the oxide layer on the surface of the feedstock powder, which is naturally formed during storage. The oxide layer obstructs sound plastic deformation by consuming impact energy as it is broken. Thus, it is ideal to remove the oxide layer before deposition, although complete removal is practically impossible. Surface oxidation of metal powders is unavoidable because metals react easily with atmospheric oxygen.

Figure 5 shows the effect of surface oxidation on the critical velocity of copper, 316L stainless steel, and nickel alloy (Ref 54). With increasing oxygen content of the feedstock powder, the critical velocity increases continuously. For copper, the critical velocity rapidly develops from
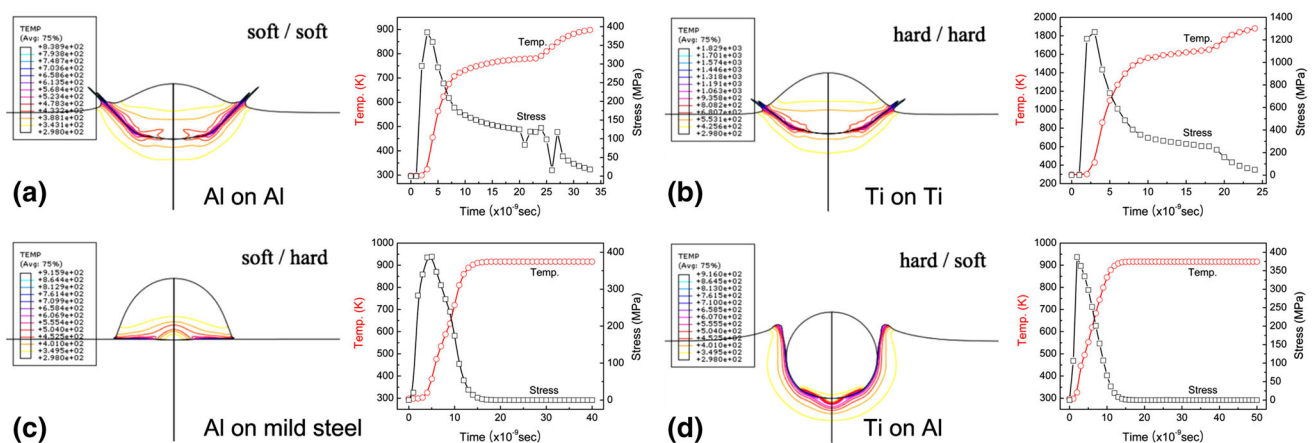

Fig. 3 Four kinds of impact behavior classified according to the relative hardness of the impacting particles and impacted substrate: (a) soft–soft, (b) hard–hard, (c) soft–hard, and (d) hard–soft (Ref 21)
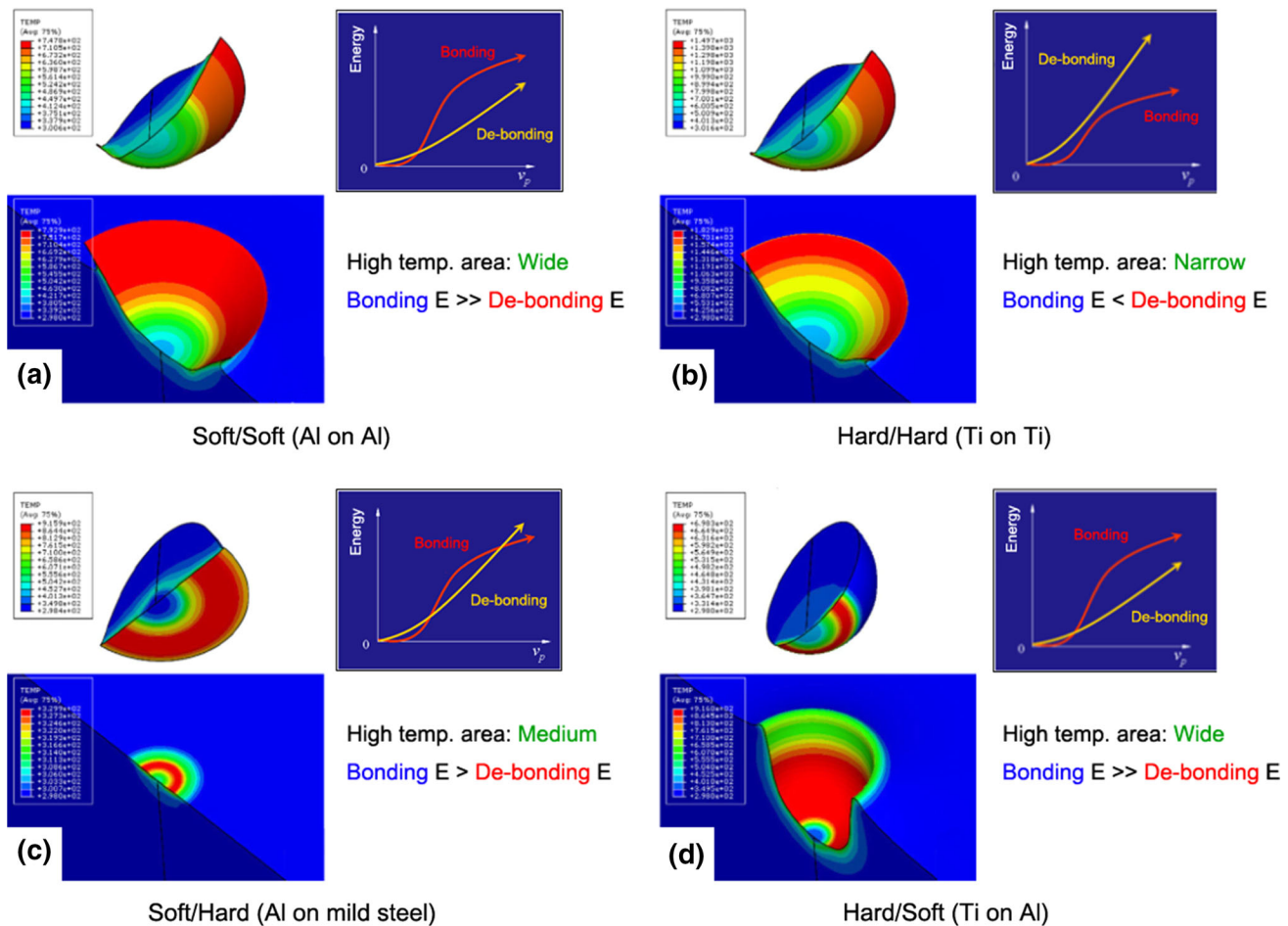
Fig. 4 Temperature distribution induced by impact for the four cases: (a) soft–soft, (b) hard–hard, (c) soft–hard, and (d) hard–soft, with corresponding adhesive/rebound energy variations vs. particle velocity (Ref 21)
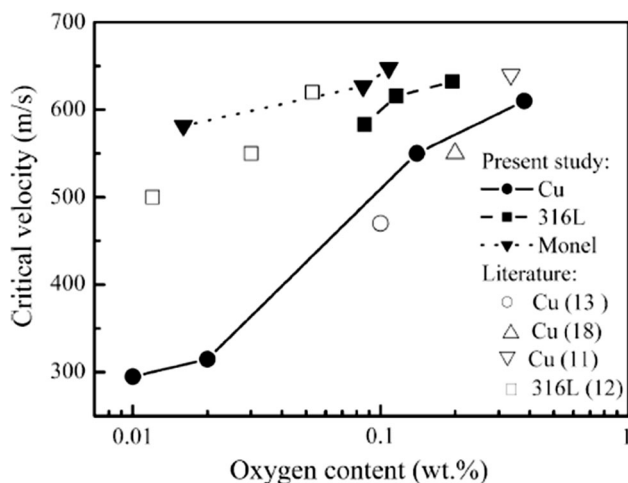

Fig. 5 Effect of surface oxidation on critical velocity of copper, 316L stainless steel, and nickel alloy (Ref 54)

310 m/s (0.02 wt.% oxygen) to 610 m/s (0.38 wt.% oxygen). Kang et al. also presented similar results in a study of the oxidation dependence of the critical velocity of aluminum

(Ref 55). The flattening ratio of the impacting Al particles decreased as the oxygen content increased (from 1.95 at 0.001 wt.% to 1.74 at 0.045 wt.%) (Fig. 6). This indicates that hindrance of plastic deformation at the interface region was intensified with increasing amount of oxides. Also, according to Ichikawa et al., when CoNiCrAlY was deposited on Inconel 625 using kinetic spraying, the deposition efficiency was degraded from 54.8 to 0.4% as the substrate surface became covered with an oxide layer (Ref 57).

In addition, the oxide layer disturbs interfacial bonding by preventing direct contact between the impact pair. It is well known that debris from broken oxides is emitted from the contact surface through the jetting phenomenon at the periphery of the interface. However, complete emission of oxide debris is impossible, and the remaining oxides interrupt bonding between the impact pair. A schematic sequence of oxide breakage at the moment of impact is shown in Fig. 7 (Ref 56). Complete extrusion of the broken oxides cannot be achieved, and some debris remains in the form of inclusions at the bonding interface. Figure 8 presents the bonding state between an Al particle and its substrate achieved in practice (Ref 55). A hollow gap was formed between the Al particle and the substrate in the
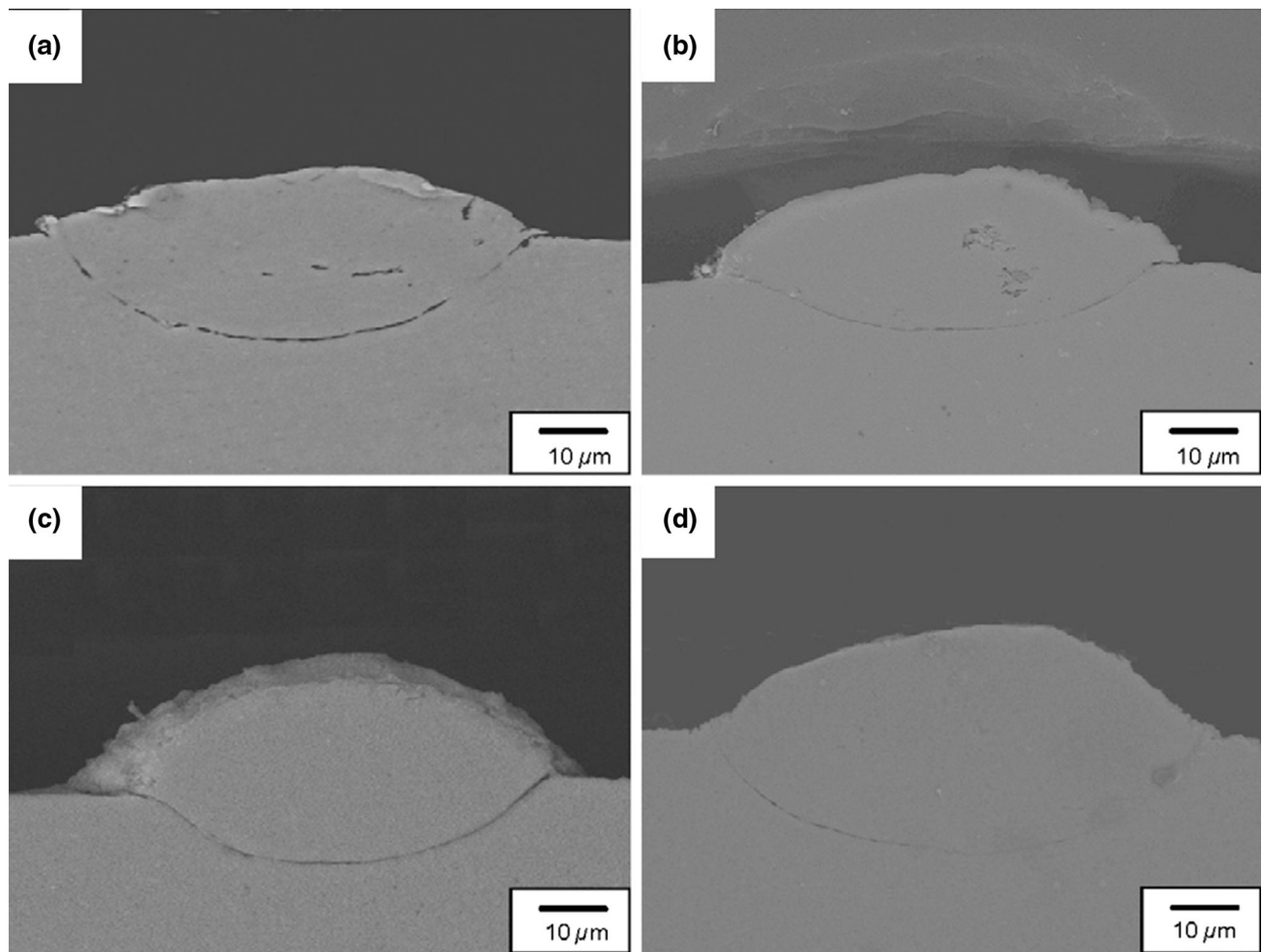
Fig. 6 Cross-sectional scanning electron microscopy (SEM) images of single deposited Al particles with oxygen content of (a) 0.001 wt.%, (b) 0.012 wt.%, (c) 0.023 wt.%, and (d) 0.045 wt.% (Ref 55)

form of pores with remaining aluminum oxides. Thus, aluminum oxides might discourage interfacial bonding by blocking contact with the bare surface.

Dynamic oxidation of the surface can also be induced during the deposition stage. Kim et al. (Ref 58) reported that the fresh surface of kinetic-sprayed Ti particles was dynamically reoxidized after breakage and ejection of the preexisting oxide layer through jet formation with adiabatic shear instability. Figure 9 shows the interfacial state of the subsequently deposited Ti particles. As shown in Fig. 9(f) and (g), an amorphous TiO_2 layer tens of nanometers thick was present in the interface region. This TiO_2 layer was newly formed rather than preexisting, because it was continuous without any trace of impact damage (Fig. 9e). It is reasonable to believe that kinetic-sprayed Ti particles could be dynamically oxidized during the deposition stage, considering that Ti and Al possess high oxygen affinity. Nonetheless, despite the oxide layer at the interface, the bonding of two subsequently deposited particles was very intimate (Fig. 9b, g). Kim et al. insisted that thin amorphous oxides do not hinder bonding of deposited particles due to their high cohesive energy to

crystalline material with a mismatched lattice (Ref 147, 148). However, a clear bonding mechanism was not discussed in their research.

2.6 Impact Angle

Generally, in the kinetic spray process, particles impact the target at an angle of ~90°, since the deposition efficiency decreases as the impact angle deviates from 90°; That is, at other angles, some portion of the impact energy is used in processes other than plastic deformation, preventing the development of adiabatic shear instability in the interface region. Of course, the tangential behavior of the impacting particles induces generation of thermal energy via friction, but its effects on bonding are inferior to those of plastic deformation with adiabatic shear instability. Figure 10 shows the degradation of the deposition efficiency and porosity for pure Ti as the impact angle deviates from 90° (Ref 60). The deposition efficiency and porosity are not degraded much until 70°, but worsen rapidly thereafter.
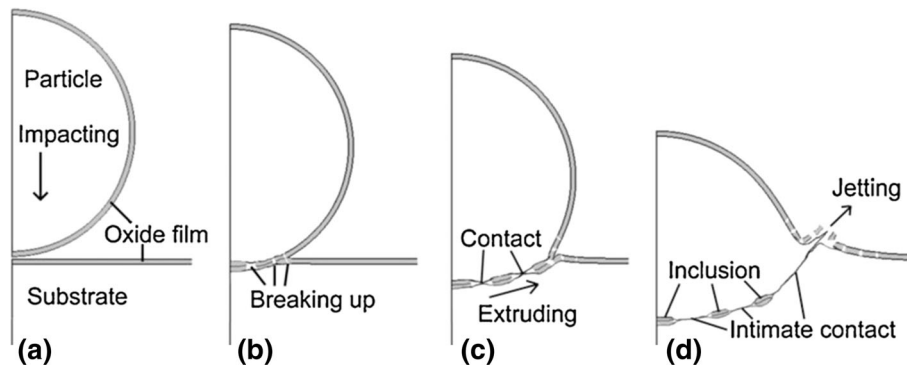
Fig. 7 Schematic diagram of break-up and extrusion of oxide layer at moment of impact in kinetic spraying (Ref 56)
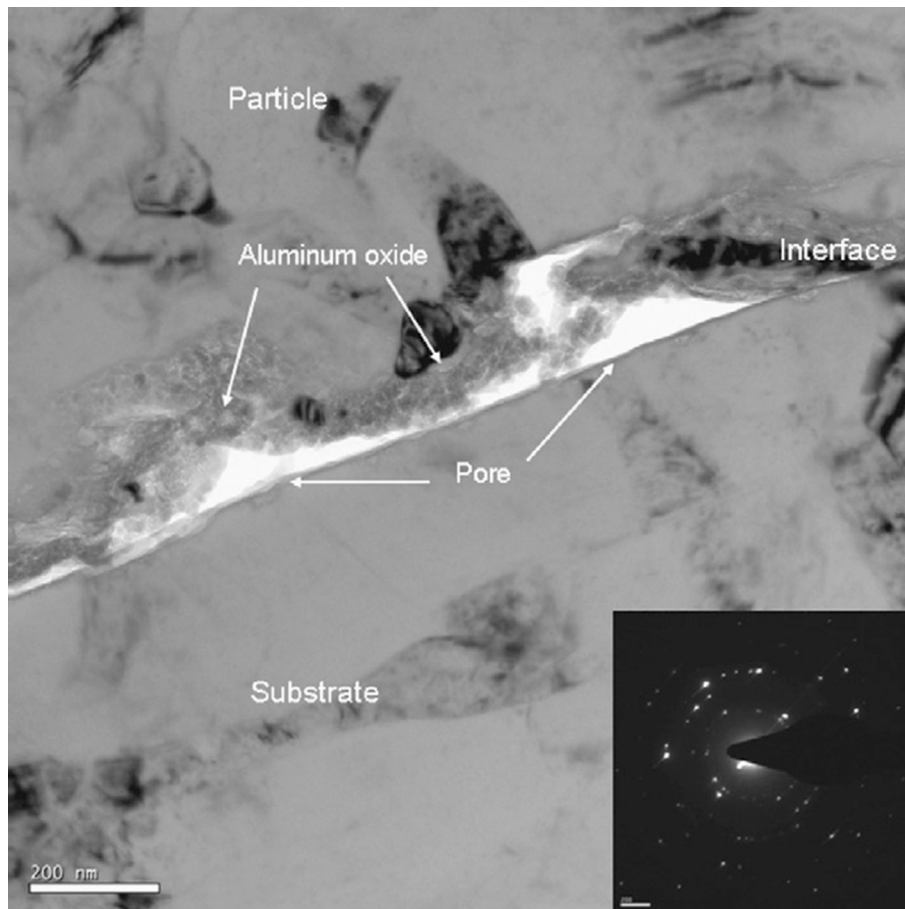

Fig. 8 Bright-field transmission electron microscopy (TEM) image of interface between kinetic-sprayed Al particles with 0.045 wt.% oxygen content (Ref 55)

Deviation of the impact angle from 90° also results in inhomogeneous particle deformation (Ref 60). As shown in Fig. 11, jetting at the particle interface edge became biased to one side as the impact angle deviated from 90°. In this case, the bonding quality was inevitably worsened because the interfacial bonding on the side with a relatively small degree of plastic deformation was poor. Thus, particles were bonded on one side, but not the other.

2.7 Interaction Between Impact Condition and Feedstock Properties

In previous sections, the effect of several impact conditions on the interface reactions in kinetic spraying was discussed. However, practically, the interface reactions depend on the interaction between the properties of the feedstock powder and the given impact conditions; For instance, criteria based on conditions such as the critical/
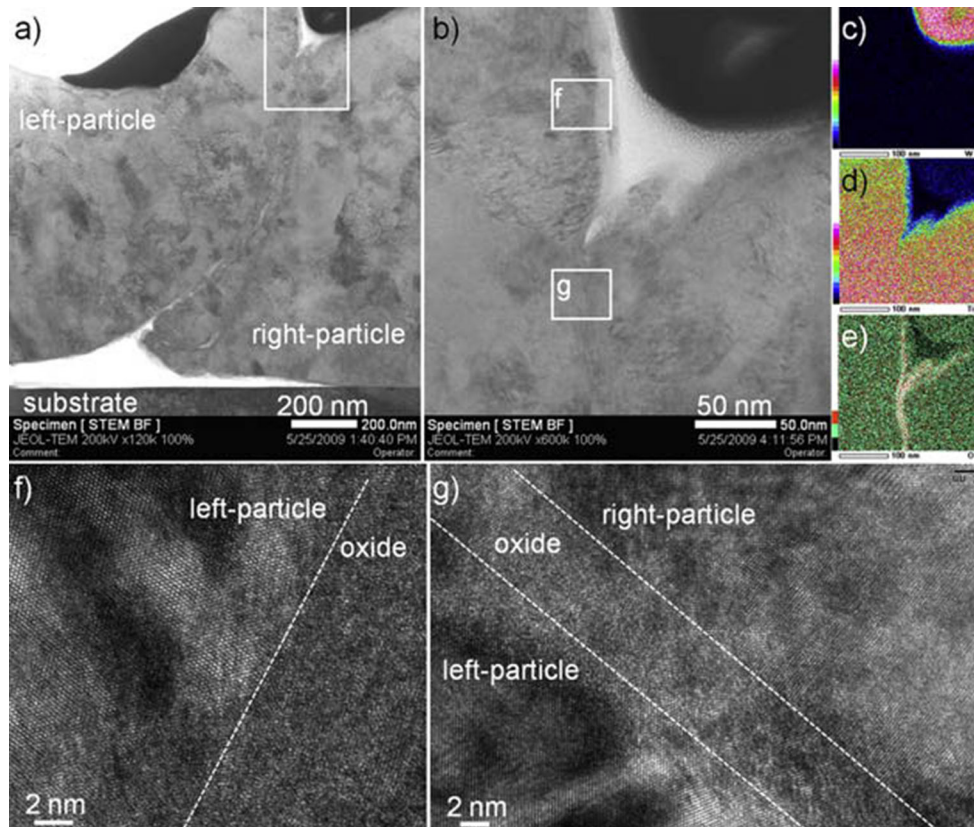
Fig. 9 Kinetic-sprayed Ti particles: (a) scanning transmission electron microscopy (STEM) bright-field image, (b) magnified image of white boxed area in (a), results of element mapping for (c) tungsten, (d) titanium, and (e) oxygen, and (f, g) high-resolution (HR) images of areas marked in (b) (Ref 58)
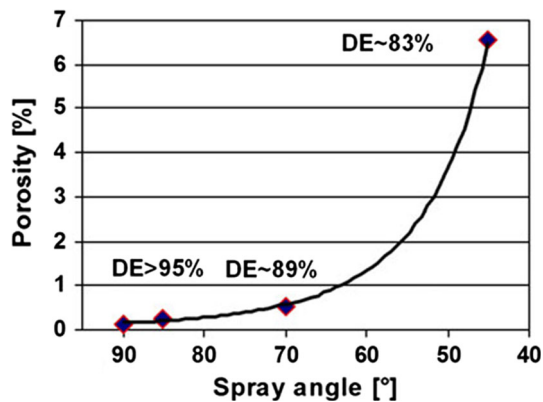

Fig. 10 Degradation of deposition efficiency and porosity for pure Ti as impact angle deviates from 90° (Ref 58)

rebound velocity, relative hardness, and degree of oxidation are determined by the material properties of the impact pair. Thus, it is helpful to understand the interactions between the impact conditions and material properties. Although all such interactions are important, only interactions between the particle velocity and material properties are discussed in this section, because the others (i.e., for relative hardness and oxidation state) are simple and obvious.

As is well known, the critical and rebound velocities result from the competition between the bonding (plastic deformation) and debonding (recoverable elastic) energies. Therefore, the interaction with respect to the particle velocity can be distinguished based on the elastic/plastic behaviors of the impact pair, which are determined by their material properties. Applying the Johnson–Cook plasticity model in a particle impact simulation using the finite-element method (FEM) allows comparison of the elastic/plastic behaviors of impact pairs, based on their elastic moduli and material-specific parameters in the equation. The Johnson–Cook plasticity model is as follows (Ref 149):

$$\sigma = \left[A + B\varepsilon_{\mathrm{p}}^{n}\right]\left[1 + C\ln\left(\frac{\dot{\varepsilon}_{\mathrm{p}}}{\dot{\varepsilon}_{0}}\right)\right]\left[1 - (T^{*})^{m}\right],$$

where σ is the equivalent flow stress, ε_{p} and $\dot{\varepsilon}_{\mathrm{p}}$ are the equivalent plastic strain and strain rate, $\dot{\varepsilon}_{0}$ is the normalizing reference strain rate, and T^{*} is the normalized temperature. A, B, C, n, and m are characteristic material parameters. A is the yield stress in a quasistatic simple tension or compression test, B is the strain-hardening coefficient, C is the dimensionless strain-rate hardening coefficient, and n and m are the power exponents of the strain-hardening and thermal-softening terms.
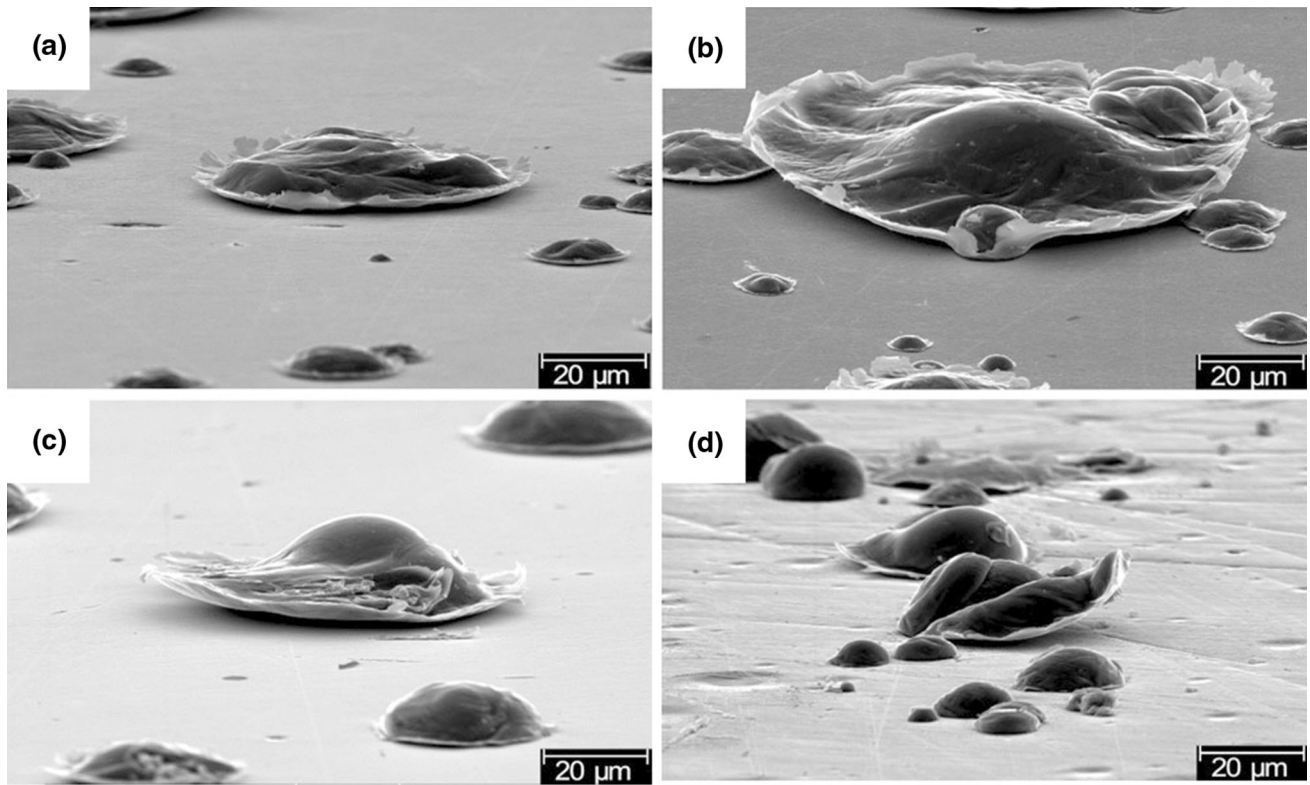
Fig. 11 Morphology of Ti particles after impact on low-carbon steel substrate (1000 °C, 4 MPa process gas) at various spray angles: (a) 90°, (b) 85°, (c) 70°, and (d) 45° (Ref 58)

Table 1   Numerical values for Ni, Ti, and Ta for particle impact simulation using FEM

	Ni	Ti	Ta
Density (kg m^{-3})	8890	4510	16,650
Young's modulus (GPa)	207	116	186
Poisson's ratio	0.31	0.34	0.35
Heat capacity (J kg^{-1} K^{-1})	456	528	153
Melting point (K)	1726	1923	3269
A (MPa)	163	806.57	340
B (MPa)	648	481.61	260
n	0.33	0.319	0.32
C	0.006	0.0194	0.042
m	1.44	0.655	0.88
Ref. temp. (K)	298	298	300
Ref. strain rate (s^{-1})	1	1	4

Table 2   Effect of each material property on deposition in particle impact simulation using FEM

	Advantageous	Disadvantageous
Density (kg m^{-3})	O	
Young's modulus (GPa)		O
Poisson's ratio	…	…
Heat capacity (J kg^{-1} K^{-1})		O
Melting point (K)		O
A (MPa)		O
B (MPa)		O
n		O
C		O
m	O	
Ref. temp. (K)	…	…
Ref. strain rate (s^{-1})	…	…

Here, Ni, Ti, and Ta are considered as representative metals. Table 1 presents their numerical values applied in a particle impact simulation using FEM (Ref 21). If the ability to be heated to near the melting point at the interface region is considered as a criterion for successful bonding, each material property can be distinguished according to whether or not it is advantageous. The influence of each material property is summarized in Table 2. Whether corresponding material property is advantageous or not is marked with symbol of 'O' in the table.

Compared with Ti and Ta, Ni has the benefit of possessing low yield strength and melting point, and a high thermal-softening exponent. However, its elastic modulus

and strain-hardening coefficient/exponent are higher than those of the other metals, which is disadvantageous for plastic deformation. Figure 12 shows kinetic-sprayed pure Ni for various process conditions. The Ni was hard to deposit successfully at 600 °C and 2.5 MPa using N$_2$ gas (condition C1) (Fig. 12a, b) (Ref 52). The point to note here is that deposition of pure Ni was not that successful even at 600 °C and 1.5 MPa with He gas (condition C2) (Fig. 12c). Also, the surface of the Ni coating layer was severely eroded by subsequent impacts from accelerated Ni particles (Fig. 12d). This indicates that the particle velocity of the later particles approached the rebound velocity of Ni, despite the relatively small difference in
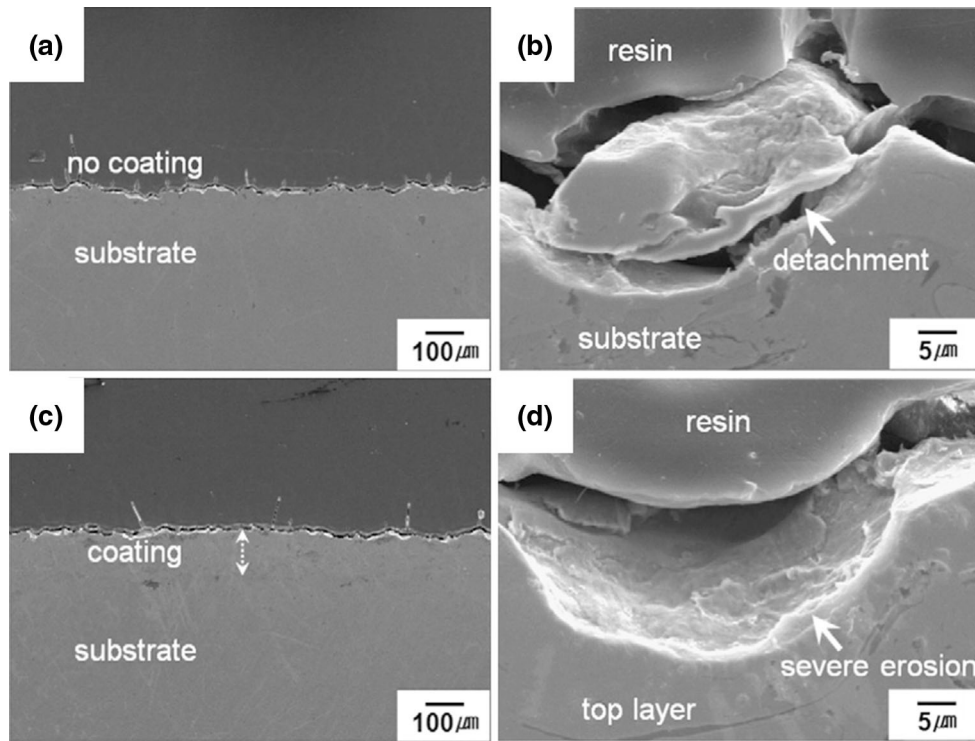
Fig. 12 Cross-sectional SEM images of kinetic-sprayed pure Ni at (a) 600 °C and 2.5 MPa with N_2 gas (condition C1) and (c) 600 °C and 1.5 MPa with He gas (condition C2), and magnified images of the top regions (b, d) shown in (a) and (c), respectively (Ref 52)

particle velocity between conditions C1 and C2 (~600 m/s and ~770 m/s, respectively). Such a narrow gap between the critical and rebound velocities implies that the effect of debonding (recoverable elastic) energy was rapidly strengthened relative to that of the bonding (plastic deformation) energy with an increase in particle velocity, indicating a powerful hardening effect. The primary cause of such a severe hardening effect is the high strain-hardening coefficient/exponent of Ni. Thus, when using Ni, it is more efficient to investigate other ways to widen the window of sprayability (WS) (Ref 20). Considering that pure Ni has a relatively high thermal-softening exponent but a low melting point, preheating the feedstock powder could be more effective than increasing the particle velocity. Figure 13 presents the stress and temperature distributions for an impact pair when using 600 °C and 2.5 MPa with N_2 gas, with and without preheating, and when using 600 °C and 1.5 MPa with He gas (Ref 52). The stress distribution is much more severe without preheating (Fig. 13a, c) than with preheating (Fig. 13b). Also, the temperature distribution in the interface region is highest among the three cases when powder preheating is applied. In practice, the coating thickness (deposition efficiency) and bond strength were dramatically improved as the preheating temperature was increased (Fig. 14). In Fig. 14(e), the coating thickness and bond strength of each pre-heating condition are presented in the form of curve and bars, respectively.

Compared with Ni and Ta, pure Ti presents almost no advantageous features, but suffers from various disadvantages (i.e., high heat capacity and yield strength, low density and thermal-softening exponent). Nevertheless,

deposition of Ti is not as difficult as it may seem, since a pure Ti layer can be fabricated even at particle velocity lower than the critical velocity reported in literature. Figure 15(a) and (d) show a Ti layer above a certain degree of thickness, despite use of a particle velocity lower than the critical velocity reported in Ref 22. Surprisingly, the deposition efficiency was about 80%, which is the value generally obtained under optimal conditions in most cases of kinetic spraying. According to Bae et al., this result was induced by the higher adiabacity of pure Ti relative to other metals (i.e. Cu, Al, Ni, and Ta). Ti retains its high adiabacity, since its thermal conductivity is lower than that of other metals (Ref 150). However, as presented in Fig. 15(a) and (d), the quality of the Ti coating layer was poor, even though deposition was achieved. To achieve a Ti layer with low density and adequate bonding, the particles should be accelerated above the critical velocity, or the critical velocity of Ti must be lowered by powder preheating. The results with powder preheating (at 600 °C) and enhanced process conditions (changing from 600 °C and 2.5 MPa with N_2 gas to 600 °C and 1.5 MPa with He) are shown in Fig. 15(b, e) and (c, f). The fabricated Ti layers became denser and the bonding state was improved in both cases. Here, the improvement in coating quality by enhancing the particle acceleration was more obvious than that achieved by powder preheating, in contrast to the case of Ni. For pure Ni, increasing the particle velocity was not optimal because of the high strain-hardening coefficient/exponent and elastic modulus of Ni. However, Ti does not possess outstanding strain and strain-rate
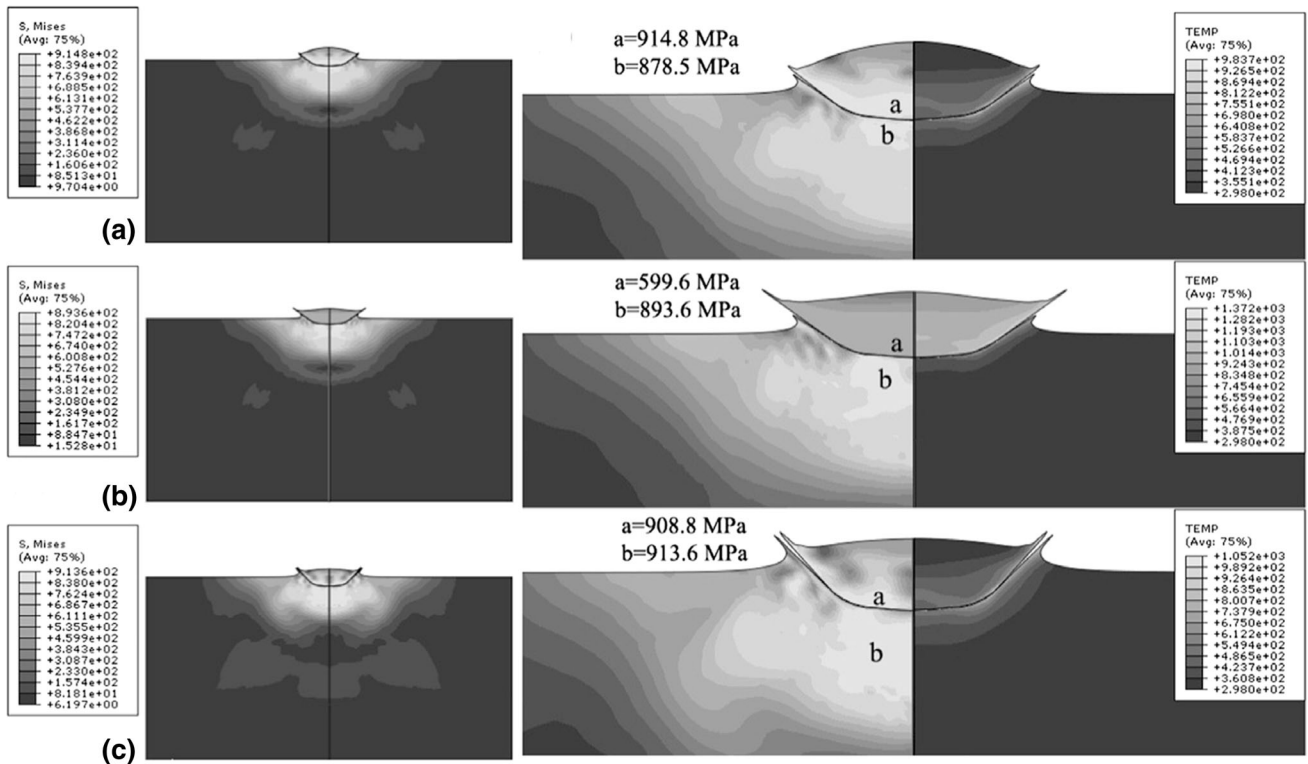
Fig. 13 von Mises stress and temperature distributions of the Ni–mild steel impact pair at 600 °C and 2.5 MPa with N_2 gas (a) with and (b) without preheating and at (c) 600 °C and 1.5 MPa with He gas (Ref 52)
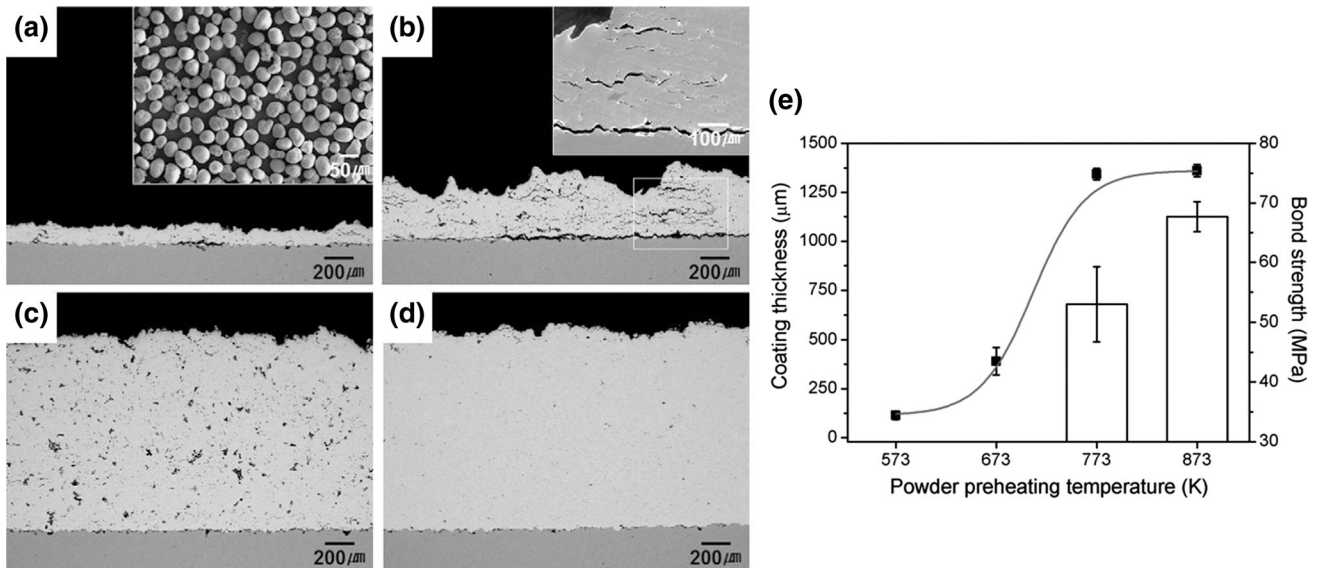

Fig. 14 Cross-sectional SEM images of kinetic-sprayed pure Ni with powder preheating at temperature of (a) 300 °C, (b) 400 °C, (c) 500 °C, and (d) 600 °C, and (e) variation in coating thickness and bond strength with powder preheating temperature (Ref 52)

coefficient/exponent. Also, the thermal-softening effect is unremarkable, because of the quite low thermal-softening exponent of Ti (0.655) relative to that of other metals (generally ~1.0). Figure 16 clearly suggests that increasing the particle acceleration is better than powder pre-

heating for improvement of the bonding of kinetic-sprayed pure Ti (Ref 22). The degree of strain and the temperature increase at the interface region were more noticeable with particle acceleration than with powder preheating.
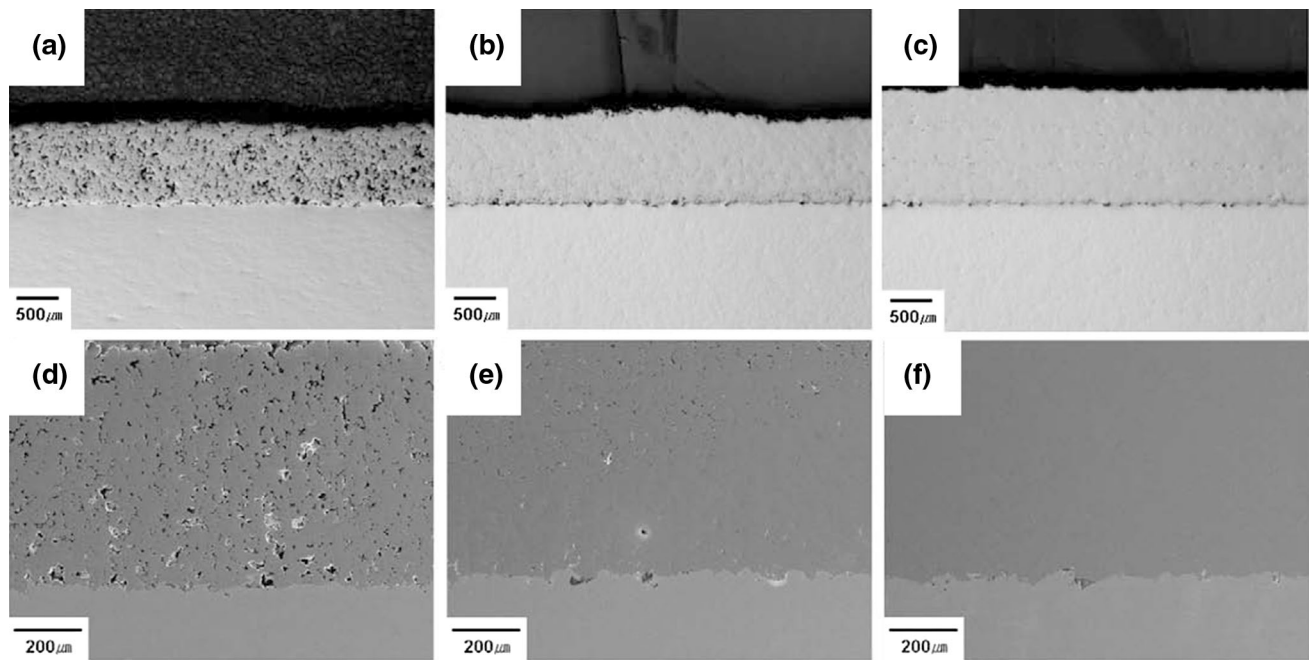
Fig. 15 Cross-sectional SEM images of kinetic-sprayed pure Ti at 600 °C and 2.5 MPa with N_2 gas (a) with and (b) without preheating at 600 °C and at (c) 600 °C and 1.5 MPa with He gas and (d–f) their magnified images (Ref 22)

Pure Ta has some advantages, such as high density and low heat capacity and strain-hardening coefficient, relative to Ni and Ti. However, its melting point and strain-rate hardening coefficient are higher than those of Ni and Ti. In particular, the extremely high melting point of Ta (3269 K) compared with Ni (1726 K) or Ti (1923) is the most important obstacle to increasing the interfacial temperature to near its melting point. Nevertheless, the critical velocity of pure Ta is ~550 m/s, including it in the group of low-critical-velocity metals compiled by Bae et al. (Ref 21). Practically speaking, pure Ta was well deposited at 550 °C and 3.0 MPa with N_2 gas when the particle velocity [numerically calculated by equation (Ref 4, 47)] was ~555 m/s (Fig. 17a). This indicates that the advantageous features of Ta (i.e., high density, low heat capacity and strain-hardening coefficient) dominate its disadvantageous features (i.e., high melting point and strain-rate hardening coefficient), resulting in a relatively low critical velocity. However, although a certain degree of deposition was achieved, the deposition efficiency of pure Ta developed from ~50 % to more than 80 % on enhancement of the process conditions (from 550 °C and 3.0 MPa with N_2 gas to 550 °C and 2.0 MPa with He gas) and powder preheating (Fig. 17f). Here, in Fig. 17(f), bars are corresponding to the wt.% of O and N elements, and upper and lower curves are relevant to the deposition efficiency and hardness, respectively. The point to note here is that powder preheating was more effective than enhancing the process conditions, probably because of the high strain-rate hardening coefficient of Ta.

In summary, whether an interaction that is beneficial for successful deposition will be induced is determined by the impact conditions and material properties of the feedstock powder. Even though these interactions cannot be obviously classified into certain types for all metals, some predictions can be deduced using the material-specific parameters of the Johnson–Cook plasticity model and the general properties (i.e., density, heat capacity/conductivity, melting point, and elastic modulus) of the metal feedstock powder.

2.8 Summary

As discussed above, interface reactions in kinetic spray technology are strongly affected by the impact conditions (i.e., particle velocity, particle and substrate temperatures, relative hardness of particles and substrate, oxidation state, and impact angle) and feedstock properties.

In terms of particle velocity, the interface reaction at the moment of impact can be classified into three types: (1) below critical velocity, (2) between critical velocity and rebound velocity, and (3) above rebound velocity. In case I, particles bounce off because of insufficient plastic deformation (bonding $E <$ debonding E). In case II, interfacial bonding is generated and is assisted by adiabatic shear instability (bonding $E \geq$ debonding E). In case III, bonded particles cannot withstand the rebound phenomenon due to the dominance of recoverable elastic energy (bonding $E <$ debonding E).

Preheating the particles and substrate is helpful for generating a good bonding state with relatively low particle velocity. The critical velocity for certain materials can be reduced by improving the plastic deformability by preheating the particles and substrate.

The relative hardness of the impact pair (particles and substrate) is also an influential factor and can be divided
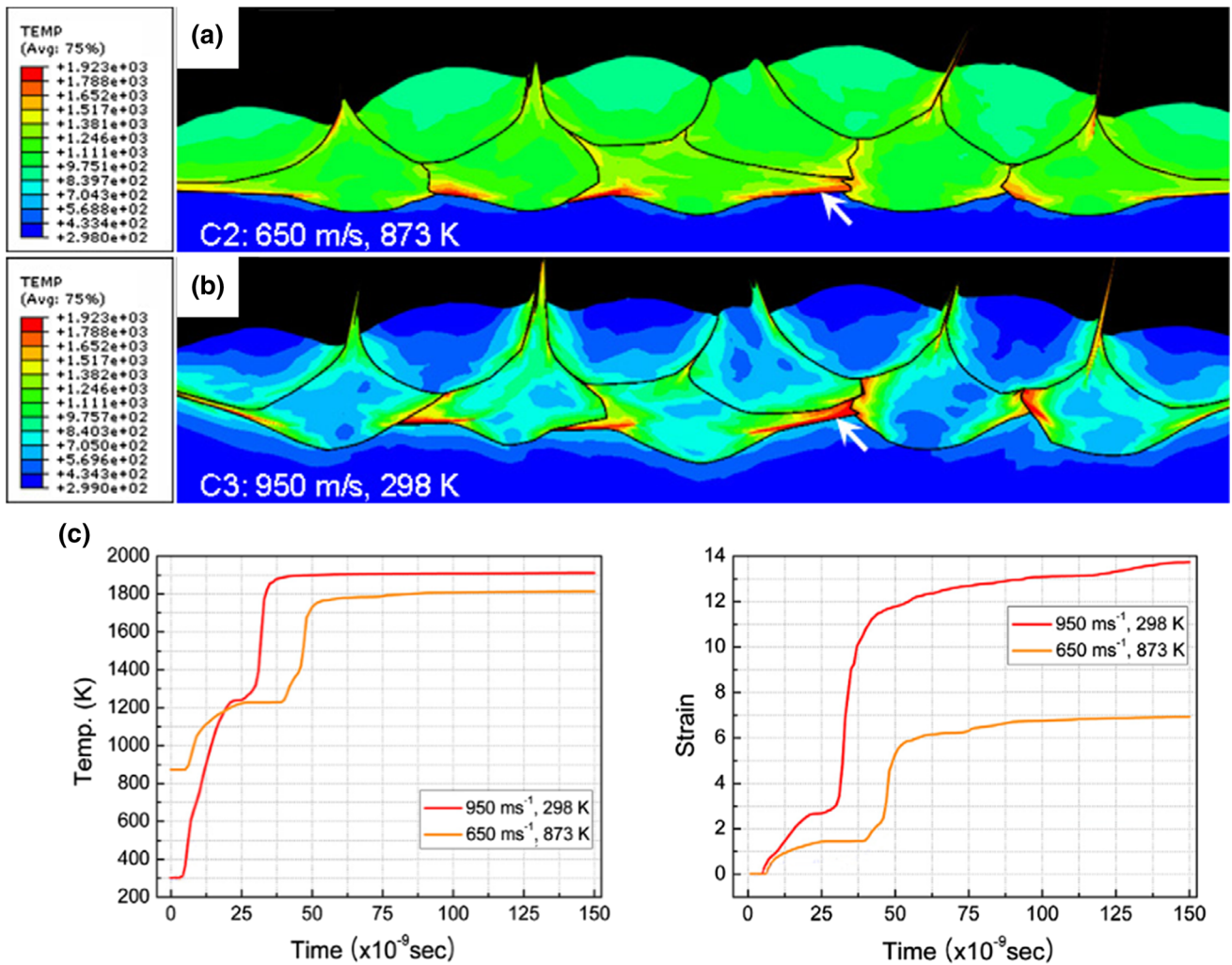
Fig. 16 Temperature distribution resulting from multiparticle impact simulation of pure Ti at (a) 600 °C and 2.5 MPa with N_2 gas with preheating at 600 °C and at (b) 600 °C and 1.5 MPa with He gas without preheating, and (c) the temperature and strain variation vs. time for (a) and (b) (Ref 22)

Fig. 17 Cross-sectional SEM images of kinetic-sprayed pure Ta under various process conditions: at 550 °C and 3.0 MPa with N_2 gas with (a) no preheating, (b) 400 °C preheating, (c) 500 °C preheating, and (d) 600 °C preheating, and (e) at 550 °C and 1.5 MPa with He gas, and (f) deposition efficiency according to nitrogen/oxygen content for each process condition

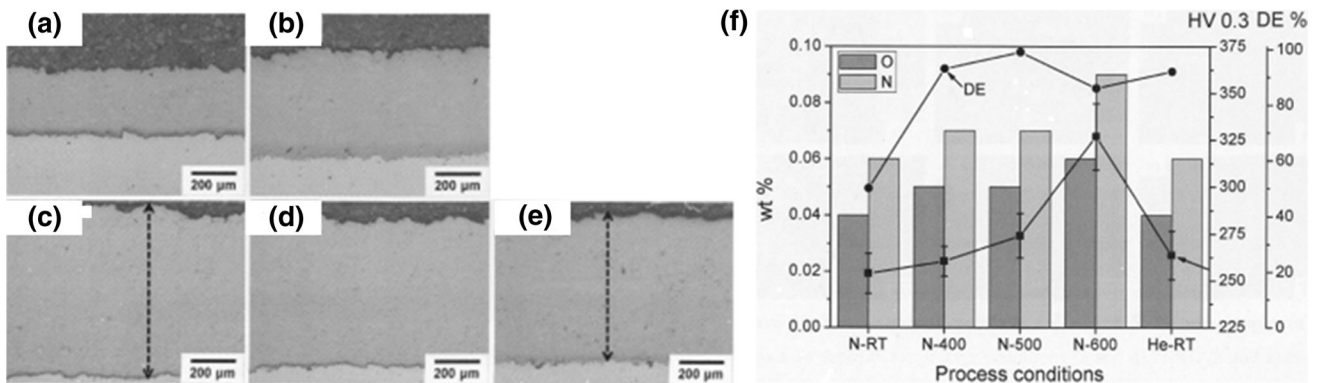into four cases: soft–soft, hard–hard, soft–hard, and hard–soft. The division of impact energy consumption differs between similar pairs (soft–soft and hard–hard) and dissimilar pairs (soft–hard and hard–soft). It is easier for dissimilar pairs to be heated to the melting point at the interface region than for similar pairs. Also, the areas of high temperature and energy development are distinct in these four cases. The area of high temperature is wider with dominance of bonding (plastic deformation) energy in the following sequence: (1) soft–soft and hard–soft cases, (2) soft–hard case, and (3) hard–hard case.

Furthermore, the effect of an oxide layer should be considered because it naturally forms on the surface of the feedstock powder during storage. The oxide layer functions as an obstacle to plastic deformation by consuming impact energy as it breaks. Also, ejection of broken oxides by jetting cannot be completely achieved, so some debris of broken oxides remaining at the bonding interface can disturb interfacial bonding by preventing direct contact between the particles and substrate.

As the impact angle deviates from 90°, the deposition efficiency degrades because of the decrease in particle impact velocity. Deviation of the impact angle from 90° also leads to inhomogeneous particle deformation, which reduces the bonding quality.

Practically, interface reactions depend on the interaction between the properties of the feedstock powder and the given impact conditions. These interactions are fairly complicated, but it is possible to compare the elastic/plastic behaviors of impact pairs based on their material-specific parameters and general properties (i.e., density, heat capacity/conductivity, melting point, and elastic modulus).

3. Dependence of Microstructural Evolution on Interface Reactions and Material Properties

3.1 Outline

The previous section presented the relationships among various impact conditions and interface reactions for different material properties. In the relationships between interface reactions and microstructural evolution, it is most important whether the induced interface reaction properly satisfies the requirements for successful bonding. With inappropriate interface reactions, bonding between impact pairs does not occur properly, and no coating layer is formed. In this section, microstructural evolution refers not to the coating layer but to the individual particles. However, since the microstructure considered in this section corresponds to a successfully fabricated coating layer, the discussion is limited to cases of interface reactions suitable to induce adequate bonding. Also, several review papers have already focused on the microstructure of the kinetic spray process (Ref 151, 152), and they can provide good understanding of the basic mechanics involved.

3.2 Inhomogeneity of Kinetic-Sprayed Deposit

In kinetic spraying, reactions directly related to bonding intensively appear at the interface region. Thus, there is always a microstructural difference between internal particles and the interface region, as visible at a glance from Fig. 18, which presents cross-sectional images of pure Cu feedstock and a kinetic-sprayed Cu deposit (Ref 74). The regions marked A-C correspond to internal particle areas, while D and E are at the interface region. The grains in the internal particle regions (A-C) are relatively well preserved compared with the feedstock particle (Fig. 18a), but those in the interface regions (D and E) are refined (Fig. 18b). Such grain refinement at the interface region must be induced by large amounts of plastic deformation and thermal energy. In most cases, grains are refined by static recovery/recrystallization (SRV/SRX) or dynamic recovery/recrystallization (DRV/DRX) (Ref 74, 77-84). Detailed discussion on grain refinement is presented in section 3.3.

Even within the interface region, the microstructure is highly distinctive according to the location (i.e., south pole and intermediate and edge parts of the particle interface region) because all the critical reactions related to bonding are induced at the periphery of the interface region. In particular, the thermal energy and stored strain energy generated at the moment of impact are specifically concentrated in the edge parts of the bonding interface due to the occurrence of adiabatic shear instability. On the other hand, at the south pole region, thermal energy is scarcely induced, and the effect of debonding (recoverable elastic) energy is dominant over the bonding (plastic deformation) energy. Figure 19 presents high-magnification images of the parts corresponding to the periphery (marked D in Fig. 18) and south pole (marked E in Fig. 18) of the interface region (Ref 74). In the periphery of the interface region (Fig. 19a), intimate bonding is generated, as seen from the indistinct particle–substrate boundary. A thin layer of nanoscale grains seems to be induced along the bonding interface by the interaction between the large amounts of thermal and stored strain energy. On the other hand, the south pole region shows a bimodal structure with an upper nanograin region and lower submicron-grain region with deformation twins (Fig. 19b). Perhaps the thermal energy was insufficient to generate recrystallization at the lower part of the south pole region, where the degree of deformation must be larger than in the upper part.

3.3 Microstructural Alteration Primarily Induced by Thermal Energy

This section mainly focuses on the microstructural evolution at the periphery of the interface region. The main point to consider here is how the feedstock material responds to the energies induced by supersonic impact. In the case of kinetic spraying, the major energies that influence the microstructural evolution are the stored strain energy and thermal energy. At the moment of deposition, the strain energy is first stored in the interface
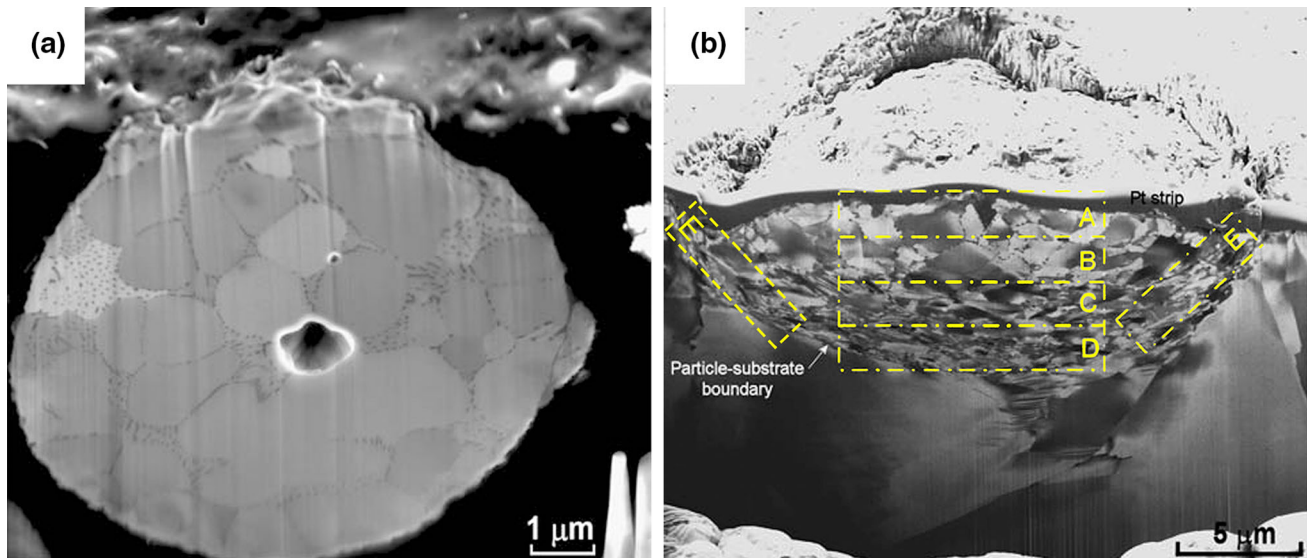
Fig. 18 Cross-sectional SEM images of (a) feedstock Cu particles and (b) kinetic-sprayed Cu particles (Ref 72)
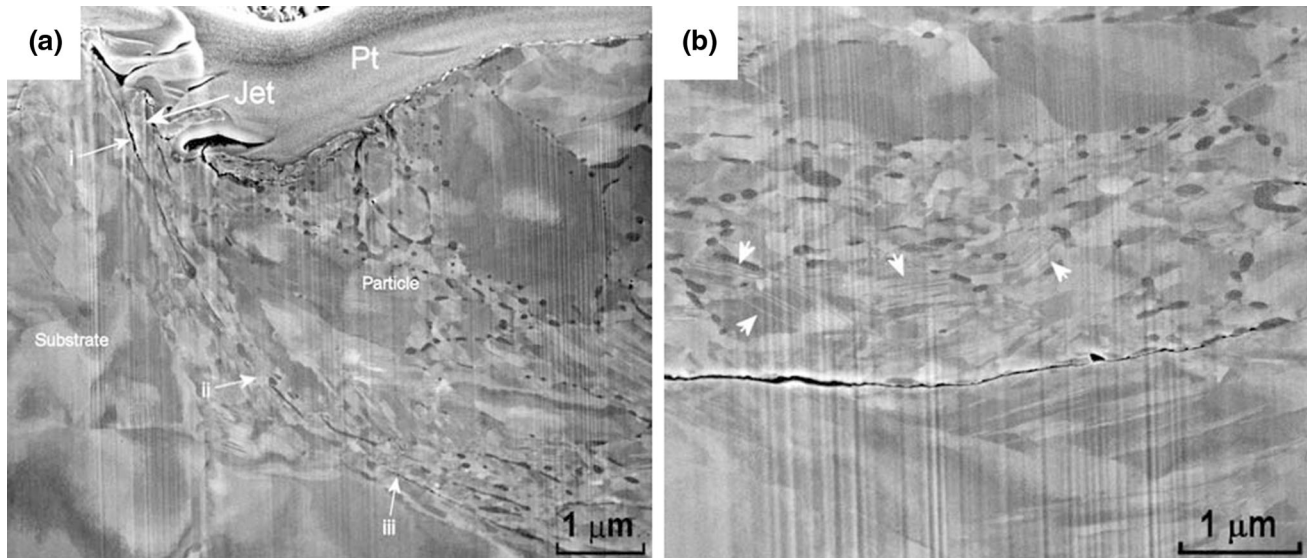

Fig. 19 Magnified cross-sectional SEM images of (a) region D and (b) region E in Fig. 16 (Ref 72)

region of the deposited particles, then thermal energy is induced in accordance with the progress of plastic deformation. Simultaneously, the feedstock powder responds to the given thermal and stored strain energy in one of two ways: (i) reacting with thermal energy or (ii) reacting with thermal and stored strain energy.

Generally, the edge of the interface region heats instantly to the melting point at the moment of successful deposition. Although the absolute quantity of induced thermal energy is insufficient to produce a reaction through a large area at the interface region, it is sufficient to generate nanoscale phase transformation and the formation of intermetallic compounds at highly localized parts of the interface. Figure 20 shows nanoscale amor-

phization of Al at the interface (Ref 85). A 3-4-nm amorphous Al layer (white box numbered 1) was created with an indistinguishable transient boundary from the amorphous to crystalline region (white box numbered 2), which seemed to be stabilized by oxygen after its formation. This amorphization primarily resulted from the rapid temperature increase to the melting point, followed by rapid quenching. Apparently, nucleation sites were crystallographic planes weakened by high-strain and strain-rate plastic deformation.

Similar to the amorphization phenomenon, localized crystallization can occur at the periphery of the interface region when amorphous material is used as the feedstock powder in kinetic spraying. Yoon et al. observed

nanocrystallization of the amorphous phase in a kinetic-sprayed deposit of CuNiTiZr (Fig. 21) (Ref 86). Crystallized CuNiTiZr appeared at the center of the amorphous region in nanoscale, as shown in Fig. 21(a) and (b). The main cause of the crystallization was induced thermal energy, assisted by a lowered activation energy resulting from high-strain and strain-rate plastic deformation. The degree of crystallization was enhanced as the process gas pressure was increased (Fig. 21c, d), providing more energy to the interface region of the CuNiTiZr deposit.

In addition, formation of nanoscale intermetallic compounds can be induced at the interface region when the kinetic spray deposition is conducted using a dissimilar impact pair (e.g., Al particles on Cu substrate). Figure 22 shows Al-Cu intermetallic compounds created at the interface in nanoscale when Al particles were successfully deposited on Cu substrate (Ref 87). Al_4Cu_9 and Al_2Cu phases with size of ~400 nm were identified by fast Fourier transform (FFT) pattern analysis in the region marked in Fig. 22. The sequence of intermetallic compound formation was as follows: (1) chemical/metallurgical bonding was created at the interface of the impact pair, (2) diffusion of elements was induced through the bonding interface, and (3) reaction occurred between the elements in the diffusion layer, assisted by the thermal energy provided by severe plastic deformation.

3.4 Microstructural Alteration Caused by Thermal and Stored Strain Energies

3.4.1 Grain Refinement and Static/Dynamic Recovery/Recrystallization. Alterations in microstructure induced primarily by thermal energy were discussed above. There

is assistance from stored strain energy, but the thermal energy effect is much more dominant in the aforementioned microstructural reactions (i.e., phase transformation and intermetallic compound formation). In this section, various microstructural evolutions dependent on both the thermal and stored mechanical energies are discussed.

As mentioned repeatedly, severe plastic deformation is induced at the interface region of kinetic-sprayed deposits, assisted by adiabatic shear instability. This plastic deformation converts a large amount of the impact energy into strain energy that is stored at the interface region in the form of defects, such as dislocations and shear bands, during the progress of deposition. This means that the interface region becomes unstable because of the high level of stored strain energy. Thus, some microstructural phenomena, such as grain refinement and static/dynamic recovery/recrystallization, stabilize the interface region, when sufficient thermal energy is available.

Grain refinement is induced dynamically during the deposition stage. In this process, countless dislocations are generated at the interface region by high-strain and strain-rate plastic deformation. Since a specific arrangement is more stable than a random dispersion, dislocation cells are created via rearrangement of dislocations. In this way, numerous subgrains are formed in the grains near the bonding interface. The sequence of grain refinement is summarized in Fig. 23, as suggested by Zou et al. (Ref 79). As shown in Fig. 23, subgrains are mainly formed along grain boundaries, where dislocations generally accumulate. The subgrains have elongated shape because of the grain refinement and plastic deformation of particles,
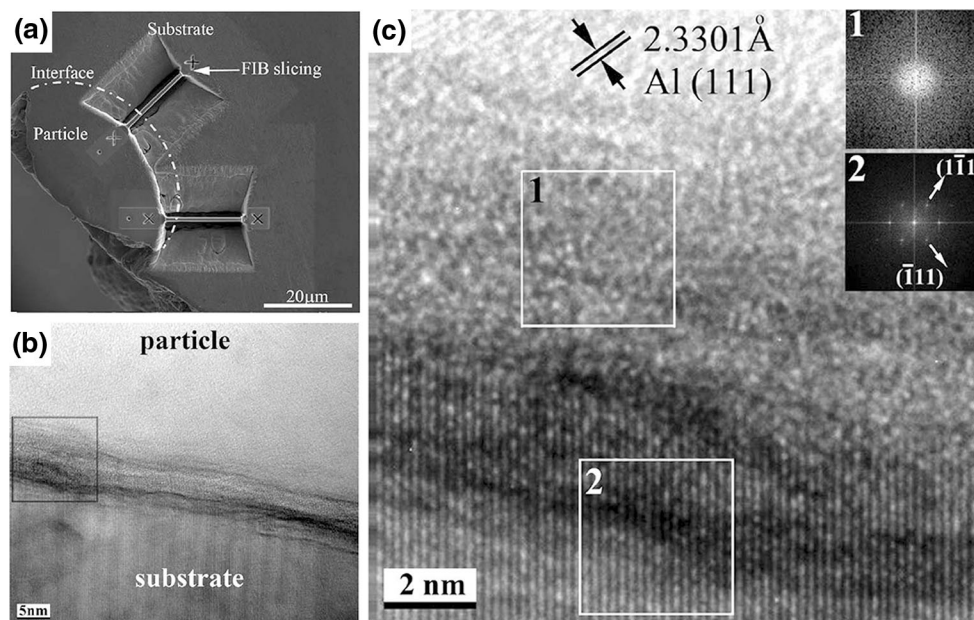

Fig. 20 TEM images at Al particle–substrate bonding interface: (a) sampled by focused ion beam (FIB), (b) high-resolution electron microscopy (HREM) image at Al particle–substrate bonding interface, and (c) highly magnified image of boxed region in (b) with fast Fourier transform (FFT) patterns of selected area (Ref 83)
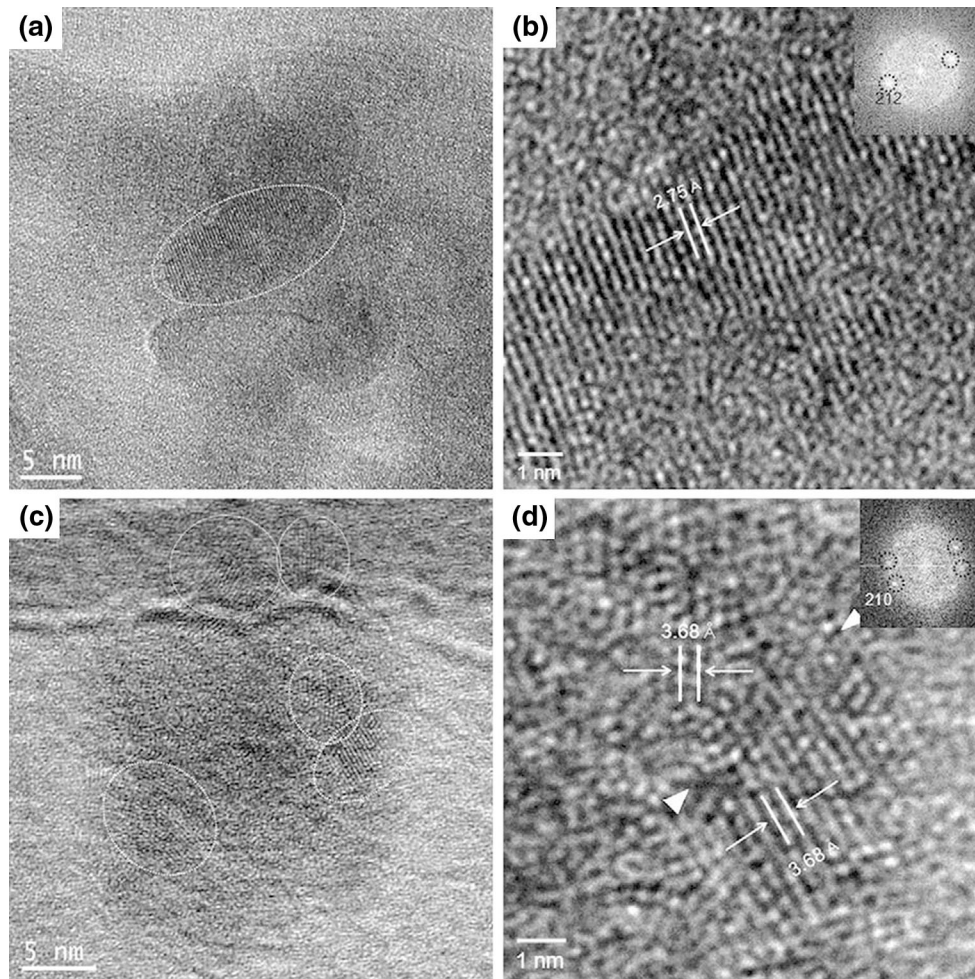
Fig. 21 HREM images of crystalline area in kinetic-sprayed CuNiTiZr deposit: (a) HREM image of nanosize crystals in Cu-based bulk metallic glass (BMG) coating (under gas pressure of 1.5 MPa), (b) highly magnified HREM image and FFT pattern in selected area of (a), (c) HREM image of nanosize crystals in Cu-based BMG coating (under gas pressure of 3.0 MPa), and (d) highly magnified HREM image and FFT pattern in selected area of (c) (Ref 84)

Fig. 22 TEM images and FFT pattern analysis of Al-Cu intermetallic compounds at the interface region: (a) TEM image of interface region and (b) highly magnified HREM images with FFT pattern of each intermetallic compound for the boxed area in (a) (Ref 85)

which can induce subsequent elongation of subgrains after their creation.

Furthermore, relief of the stored strain energy results from static/dynamic recovery/recrystallization at the interface region. Simply, DRV/DRX can be induced concurrently with deformation during the depositio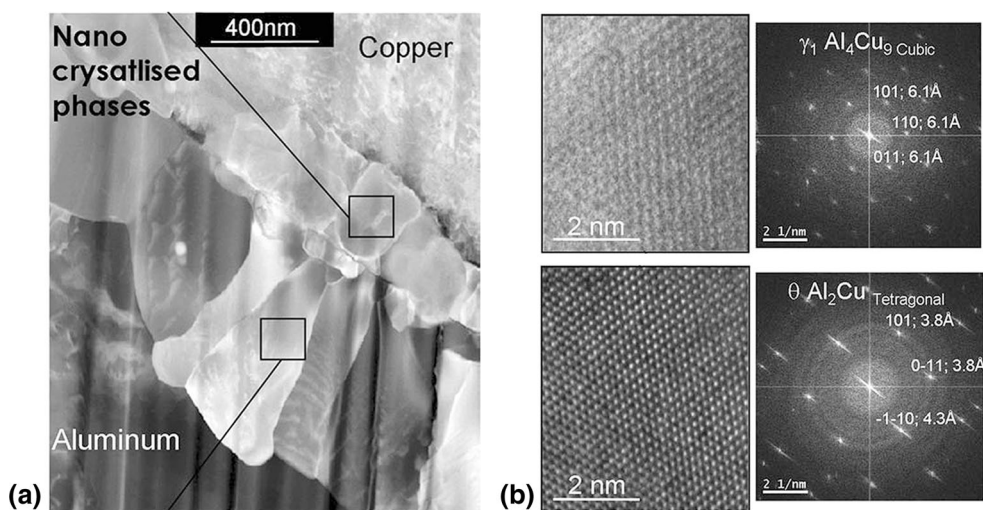n stage, and SRV/SRX can be generated at the interface region with additional thermal energy provided by subsequent particle impacts.

DRV is the phenomenon of dislocation dipole annihilation. Here, a dislocation dipole corresponds to two dislocations of opposite sign located on different slip planes. Annihilation of dislocation dipoles is primarily induced by interactions between stored network dislocations and mobile dislocations. Specifically, dislocation dipoles are annihilated by dislocation climb that results from nonzero elastic forces perpendicular to their slip planes (Ref 153-156). In the case of kinetic spraying, DRV can occur actively at the interface region because the dislocation climb phenomenon is sufficiently activated by the thermal energy induced by the severe plastic deformation.

In DRX, relief of stored strain energy is achieved by formation of dislocation-free grains. DRX induction is divided into two types according to its mechanism: migrational and rotational. Migrational DRX is primarily accomplished by migration of high-angle grain boundaries, whereas rotational DRX occurs through rotation of subgrains. For the kinetic spray process, the latter mechanism is more likely to apply than the former, because the mobility of high-angle grain boundaries is very low under high-strain-rate conditions (above $4.0 \times 10^4 \text{ s}^{-1}$) (Ref 157). When particles impact a target in kinetic spraying, the strain rate of plastic deformation at the interface region definitely exceeds the strain-rate criterion for mobility of high-angle grain boundaries. Thus, it is reasonable to explain DRX at the interface region in a kinetic spray process using the theory of rotational DRX. Zou et al. explained the detailed sequence of rotational DRX in kinetic spraying (Fig. 24) (Ref 79). Numerous subgrains are created by the grain refinement phenomenon near grain boundaries (Fig. 24a). Afterwards, the created subgrains are broken into much smaller pieces, as the plastic deformation of the impacted particles progresses, even after the formation of subgrains (Fig. 24b). Consequently, the broken pieces of subgrains are rotated by continuous exertion of shear forces, and strain-free grains are formed with high-angle grain boundaries (Fig. 24c).

SRV and SRX in the kinetic spray process are generated by residual heat or additional supply of thermal energy from subsequent particle impacts. In the case of residual heat, SRV/SRX progresses during the cooling stage after adiabatic heating of the interface at the moment of deposition. In this case, the residual heat needs to be maintained for a sufficiently long time. Therefore, occurrence of SRV/SRX is more likely in high-adiabacity (low thermal conductivity) materials such as Ti. Here, the adiabacity indicates how long a material retains the generated thermal energy in a specific region. Thus, for SRV/SRX via additional supply of thermal energy, heat is provided by additional plastic deformation of a predeposited layer through successive particle impacts or through transfer from the upper deposited layer of subsequent particles. In this case, SRV and SRX can occur even in materials with high thermal conductivity (e.g., Al and Cu). The additional plastic deformation from subsequent particle impacts has to be sufficient in terms of quantity and persistence. According to Kang et al., SRV and SRX occur in sequence (Fig. 25) (Ref 77). As shown in Fig. 25(a), SRV and SRX are not induced in the moment preceding deposition, and only some parts of the lower bonding interface experience DRV or DRX. However, when deposition of subsequent particles occurs, heat is generated by additional plastic deformation of the predeposited layer and is transferred from the upper deposited layer (Fig. 25b). As a result, static restoration (SRV/SRX) occurs in regions with strain energy induced by the impact of subsequent particles above a certain threshold (Fig. 25c).

3.4.2 Different Microstructural Responses According to Material Properties. As explained above, grain refinement and static/dynamic restoration phenomena can arise at the interface region if it retains a high degree of strain energy induced by high-strain and strain-rate plastic deformation. However, the definitive microstructural evolution is determined by the interaction of the given thermal and stored strain energies with the material properties of the particular feedstock powder. All such interactions cannot be classified completely into specific cases, but one point of obvious importance is whether the energy requirements are satisfied to induce an alteration in the microstructure of a given feedstock material. Hence, it is helpful to examine practical cases to understand the microstructural relationship and predict the microstructural changes.

Figure 26 shows the microstructure near the interface region of kinetic-sprayed Ni, Ti, and Ta layers (Ref 78, 79). In all cases, refined microstructures appeared along the bonding interface. Although refinement of the
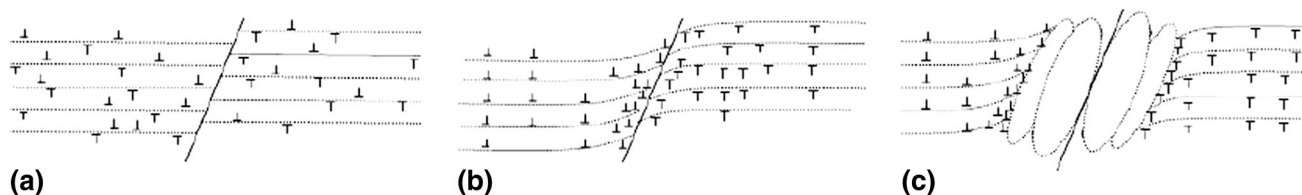

Fig. 23 Sequence of subgrain formation: (a) nondeformed microstructure with low dislocation density, (b) accumulation of dislocations with shearing, and (c) resultant grain refinement with formation of elongated subgrains (Ref 77)
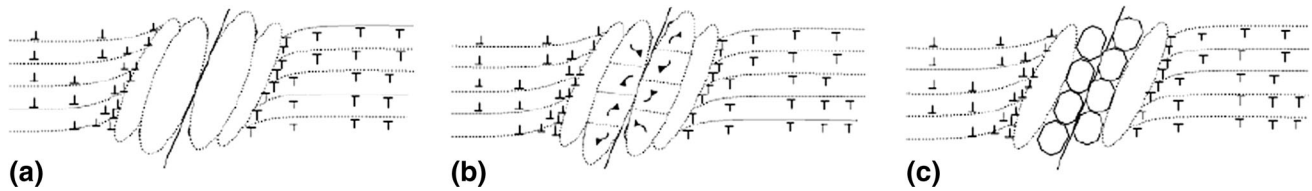
Fig. 24 Sequence of rotational DRX: (a) formation of elongated subgrains, (b) break-up of elongated subgrains, and (c) rotation of broken pieces from subgrains (Ref 77)
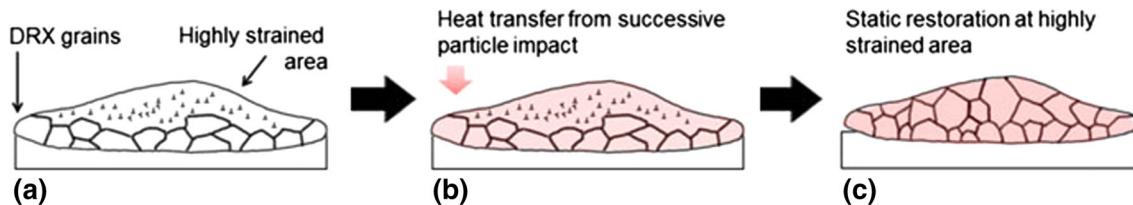

Fig. 25 Sequence of SRV and SRX by impact of subsequent particles: (a) microstructural state after deposition of first layer, (b) additional heating by impact of subsequent particles, and (c) occurrence of SRV and SRX using provided thermal energy (Ref 75)

microstructure can be induced by both static and dynamic restoration, it is obvious that such grain refinement was caused by DRV/DRX rather than SRV/SRX. Almost no strain or defects appear in newly created refined grains produced by SRV and SRX. However, it is obvious that a considerable number of defects remained in the refined grains nearby, which were apparently generated after grain refinement (left side of Fig. 26a). In the case of the grains created by DRV and DRX, generation of additional defects in the grains was inevitable because plastic deformation proceeds simultaneously with DRV/DRX, as shown clearly in the pattern quality map of kinetic-sprayed Ni obtained by electron backscatter diffraction (EBSD) (right side of Fig. 26a) (Ref 79). The pattern quality of the newly formed nanograins was extremely poor, which means there were a significant number of defects in the refined grains near the interface region. Strain-free grains were also rare in the kinetic-sprayed Ti and Ta deposits (left side of Fig. 26b and c) (Ref 78). However, particularly for Ti, some dislocation-free nanograins (~10–100 nm) were found very near the bonding interface (right side of Fig. 26b) (Ref 78). Such nearly nondefective grains might have been created by static restoration. As explained in section 3.4.1, SRV and SRX can be induced in materials that possess high adiabacity, which can retain the thermal energy resulting from plastic deformation for a sufficiently long time during the cooling stage of the deposited particles.

The microstructures in the interface region for face-centered cubic (FCC) metals (Al, Ni, and Cu) are presented in Fig. 27 (Ref 83). Although Al, Ni, and Cu share the same crystal structure, the freedom of dislocation movement varies among them and critically influences strain restoration. Thus, the stacking fault energy (SFE) can significantly influence the microstructural evolution in the kinetic spray process, since the dislocation movement and interaction among dislocations vary according to the SFE of the feedstock powder. Therefore, the microstruc-

tures of Al, Ni, and Cu are distinctive from one another, as shown in Fig. 27. In the Al deposit, an equiaxed nanocrystalline structure was created (marked C in Fig. 27a), which must have been the result of static/dynamic restoration at the moment of deposition. However, recovery and recrystallization have a competitive relationship, because both are driven by consumption of stored strain energy. It is therefore unavoidable that one will be inferior when the other is superior. In the case of Al, the feedstock metal with the highest SFE, creation of a stacking fault plane can increase the energy state considerably (Ref 83). Compared with Ni and Cu, dislocations generated in Al are difficult to dissociate in particle dislocations due to the high SFE, guaranteeing freedom of dislocation movement. Thus, in Al, recovery is preferred over recrystallization, because of its dependence on dislocation movement. It is more reasonable to conclude that the grain refinement in the kinetic-sprayed Al deposit was induced by recovery rather than recrystallization. A tangled structure corresponding to regions A and B in Fig. 27(a) was also observed.

On the other hand, Ni possesses lower SFE than Al, so recrystallization becomes more competitive with recovery than for Al. The refined structure on the left side of Fig. 27(b) might have been created by both recovery and recrystallization, although Borchers et al. insisted that the restoration was mainly caused by recrystallization (Ref 83). Interestingly, coffee-bean-like structures appear on the right side of Fig. 27(b). According to Borchers et al., this characteristic microstructure is formed when intrinsic/extrinsic dislocation loops are generated in the grains (Ref 158). Intrinsic/extrinsic dislocation loops are created by agglomeration of point defects and are assisted by dislocation climbing.

In the case of kinetic-sprayed Cu deposits, recovery is restrained by its low SFE (relative to Ni and Al). In this case, phenomena that depend on dislocation movement (i.e., cross-slip and recovery) rarely arise because of the
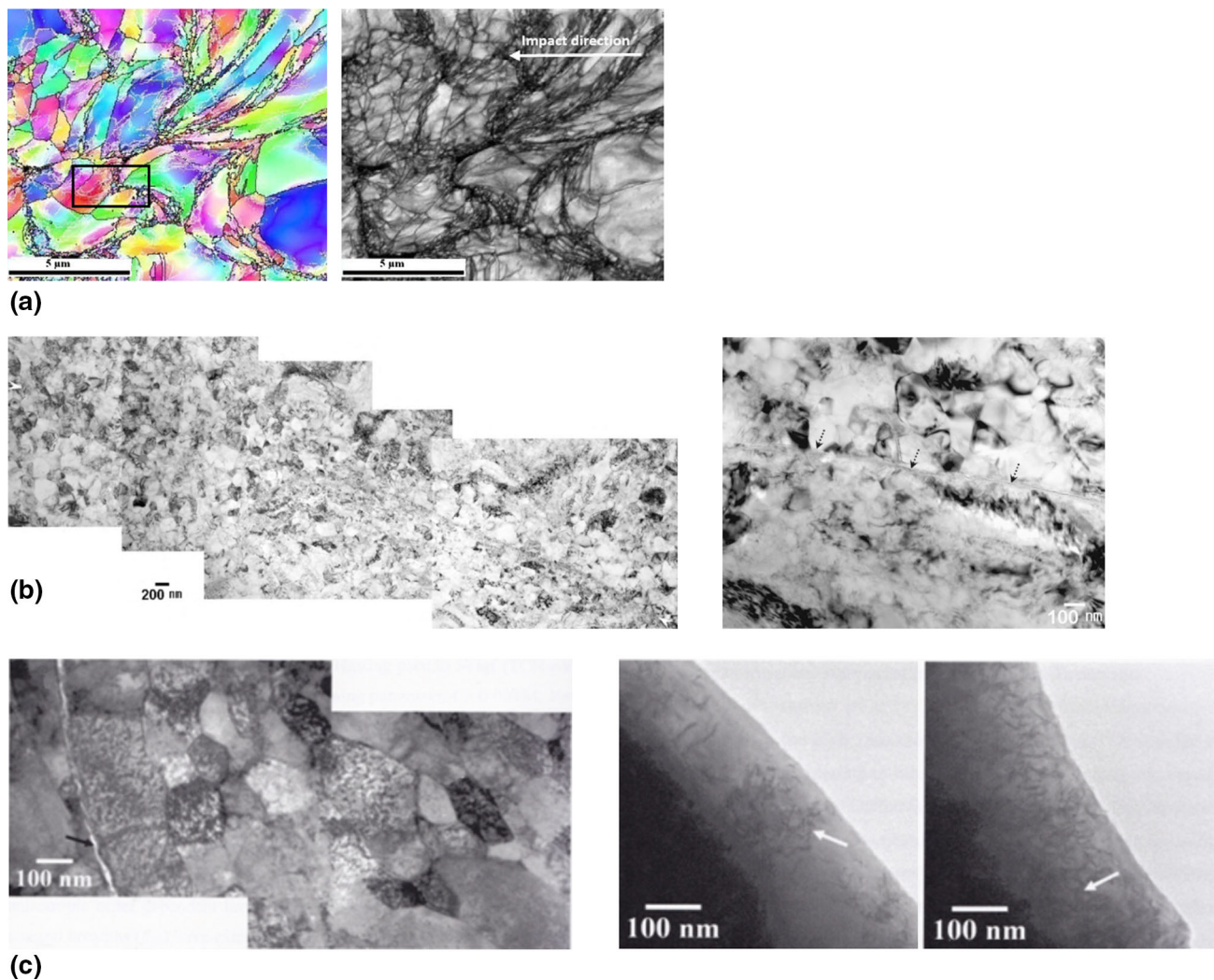
Fig. 26 Microstructural images of kinetic-sprayed Ni, Ti, and Ta coating layers: (a) EBSD characterization of Ni deposit; Euler angle map (left) and pattern quality map (right) (Ref 77), (b) TEM images of kinetic-sprayed Ti deposit and the particle–particle interface region (left), and magnified bright-field images with dislocation-free small grains marked with black dotted arrow (right) (Ref 76), and (c) TEM images of kinetic-sprayed Ta deposition and the particle–substrate interface region (left) and tangled dislocations (right)

frequent dissociation of dislocations that involve creation of stacking fault planes (Ref 83). Thus, recrystallization must have been the primary phenomenon in the Cu deposit. However, since recrystallization is sensitive to local conditions such as dislocation density/orientation/arrangement and temperature, the microstructural evolution is quite distinctive with respect to the local conditions even within the same interface region. Figure 27(c) shows the complicated organization of microstructures in a kinetic-sprayed Cu deposit: large grains whose walls consist of countless dislocations (A), elongated refined grains (B), equiaxed nanocrystalline grains (C), and micrograins with recrystallization twins.

Thus, the microstructural evolution differs case by case. In accordance with local conditions and material properties, a dominant mechanism of restoration that forms characteristic microstructures, such as the coffee-bean-like structure in Ni, can be determined. Other distinct

microstructures can also be induced in the kinetic-sprayed coating layer (Ref 158-160), but those details are not dealt with here. In the next section, the effects of various microstructures in kinetic spraying on the mechanical properties are discussed in order of importance.

3.5 Summary

As discussed above, the microstructural features in kinetic-sprayed layers result primarily from the generation of high-strain and strain-rate deformation, which instantly induces large amounts of thermal energy at the interface region. Basically, microstructural differences always exist between internal particle and interface regions in kinetic-sprayed deposits because plastic deformation and the rise of thermal energy are limited to the interface region. However, even within the interface region, the microstructure varies considerably by location (i.e., south
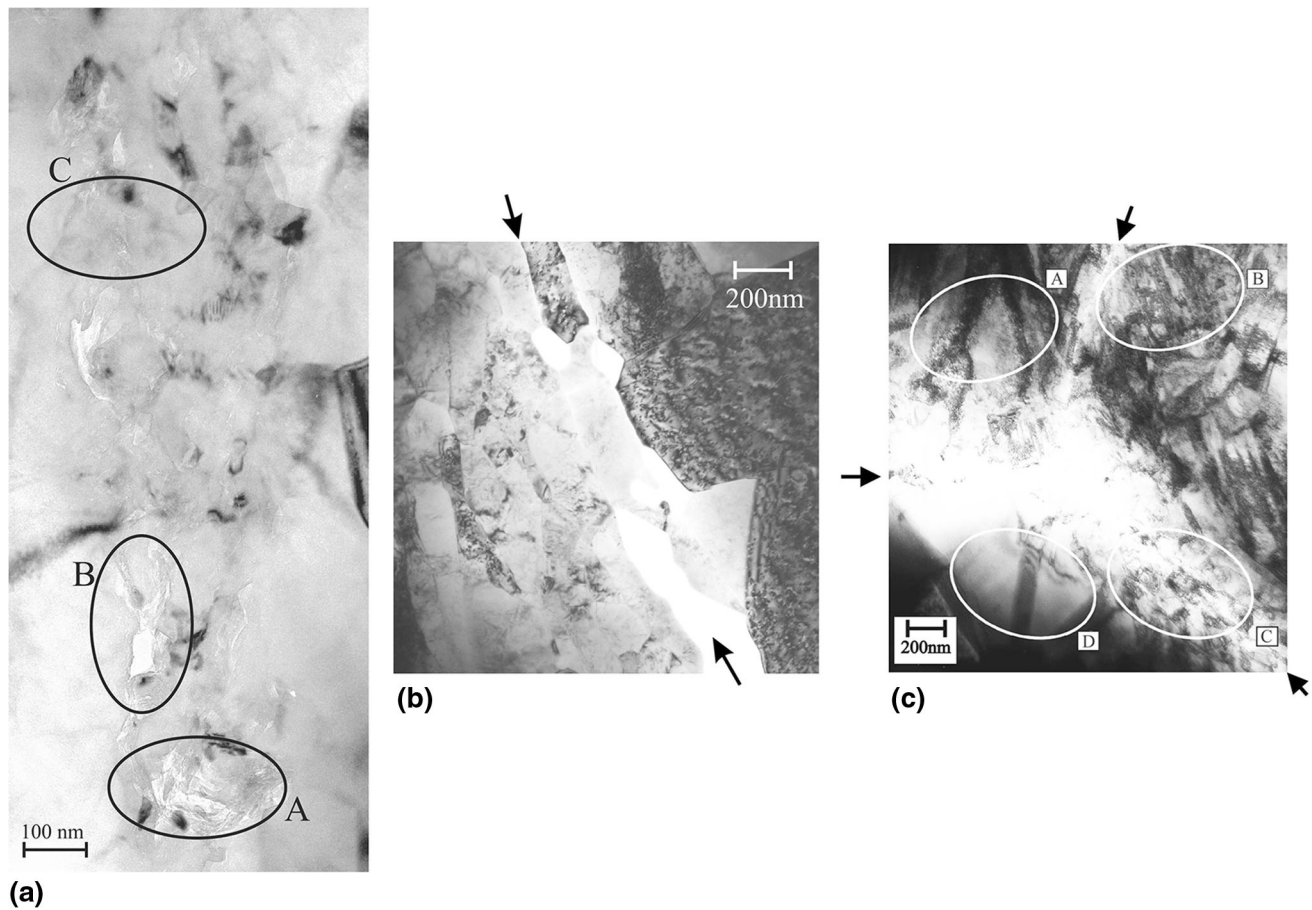
Fig. 27 TEM images of kinetic-sprayed Al, Cu, and Ni deposits: (a) particle–particle boundary region of Al deposit, (b) particle–particle boundary region of Ni deposit with interparticle boundaries marked with black arrows, and (c) triple joint of deposited Cu particles with interparticle boundaries marked by black arrows (Ref 81)

pole, intermediate and edge parts of the particle interface region), since most of the critical reactions related to bonding are induced only at the periphery of the interface; For instance, at the periphery of the interface region, a thin layer of many nanoscale grains can appear along the bonding interface, while the south pole region shows a bimodal structure or relatively coarse, microscale structures.

Specifically, microstructural alterations can occur in two ways in accordance with the type of energy required: (i) thermal energy and (ii) thermal and stored strain energy. In case I, the microstructure is altered when the edge part of the interface region is instantly heated to the melting point. Although the absolute quantity of induced thermal energy is insufficient to produce a reaction across a large area of the interface region, it is sufficient to generate several reactions (i.e., phase transformation and formation of intermetallic compounds) in highly localized areas in nanoscale. In case II, some microstructural phenomena, such as grain refinement and static/dynamic recovery/recrystallization, stabilize the interface region when sufficient thermal energy is provided to relieve the high level of stored strain energy that results from the severe plastic deformation. Specific forms of microstruc-

tural evolution are determined by the interactions between the given thermal and stored strain energies and the material properties of the feedstock powder. Not all interactions can be classified into specific cases, but whether the specific energy requirements are satisfied for certain materials is obvious.

4. Distinctive Features of Mechanical Properties Induced by Characteristic Microstructural Evolution at the Interface Area

As explained in section 3, a remarkable characteristic of the microstructures in kinetic-sprayed metal deposits is that nanoscale grains are created by grain refinement and static/dynamic restoration. When a nanocrystalline structure is created, the mechanical behavior of the material changes from that of a microscale structure. In kinetic spraying, the hardness is greatly improved by grain-boundary strengthening (Hall–Petch relationship) due to the generation of ultrafine (100-500 nm) grains with a

certain amount of internal dislocations that result from DRV and DRX. Such enhancement of the hardness is assisted by the high density of dislocations far from the bonding interface that is not relieved by static/dynamic restoration because of insufficient thermal energy supply. Zou et al. (Ref 84) and Bae et al. (Ref 52) confirmed this hardness increase at the interface region. According to Zou et al. (Ref 84), the hardness of the interface region was much higher than that of the internal region. For kinetic-sprayed Ni deposit, the average hardness at the interface region was 4.3 GPa, whereas that of the internal region was 3.3 GPa (Fig. 28). They calculated the numerical value of hardness using $H = H_i + H_{\Delta GB} + H_{\Delta\rho} = H_i + H_{\Delta GB} + 3\sqrt{3}\alpha\mu b\sqrt{\Delta\rho}$, to confirm that the primary reason for the increase of hardness was the grain boundary and strain hardening phenomena. Although $H_{\Delta GB}$ and $H_{\Delta\rho}$ were not precisely estimated, the hardness at the interface region calculated assuming $H_{\Delta GB} = \sim 1$ GPa (Ref 159, 160) and $\Delta\rho = 2 \times 10^{14}$ m^{-2} (Ref 161) (i.e., 4.6 ± 0.2 GPa) was similar to the experimental result (4.3 GPa). Additionally, Bae et al. (Ref 52) verified that the maximum nanohardness of a kinetic-sprayed Ni deposit (~5.5 GPa) was adequately high, similar to that of electrodeposited ~20-nm nanocrystalline Ni (5.1-6.0 GPa) (Ref 162), though they both had lower hardness than ~6-nm nanocrystalline Ni (7.6-9.7 GPa) (Ref 163).

Nanocrystalline (~30-100 nm) grains smaller than ultrafine (100-500 nm) grains can be created at the interface region by SRV and SRX. At this scale, plastic deformation is encouraged by behavior involving grain boundaries rather than by dislocation movement (i.e., grain boundary sliding, GBS) (Ref 164). Dislocations cannot be generated in nanograins, since the equilibrium distance between dislocations is larger than the size of the grains, which is called *dislocation pile-up breakdown*. Bae et al. (Ref 78) reported evidence of GBS in a kinetic-sprayed specimen. Figure 29 shows the morphology of a transparticle fracture surface in a kinetic-sprayed Ni layer.

Obviously, many nanosized dimples resulted from GBS among high-angle grain boundaries (HABs) during plastic deformation. In this case, the material can acquire superplasticity, where extraordinary ductility appears during plastic deformation within a certain range of strain rate and elevated temperature. However, no research has yet focused on the superplasticity behavior of kinetic-sprayed metal deposits.

The most interesting characteristic of kinetic-sprayed metal coating layers is the coexistence of ultrafine (100-500 nm) grains with nanocrystalline (~30-100 nm) structures at the interface region. As presented in Fig. 30 (marked with black dotted circle) (Ref 78), a bimodal structure of ultrafine grains and nanocrystalline structures shows both excellent hardness and ductility (Ref 165-167).

However, these advanced mechanical properties are only reasonable in the interface region. Within the whole coating layer, the bonding interface is usually imperfect because of defects such as porosity and cracks induced by the supersonic impacts. These flaws significantly degrade the mechanical properties of a kinetic-sprayed metal deposit by serving as starting points for cracks. Table 3 presents the mean hardness of kinetic-sprayed Ti deposits under various process conditions as measured by the indentation method (Ref 111). All the specimens possessed higher nanohardness than bulk Ti, but only a few of them presented advanced microhardness relative to bulk Ti when the particle velocity was above a certain threshold. Here, the nanohardness values were calibrated using Eq 1 to minimize the effect of indentation load and size.

$$H = H_0\sqrt{1 + \frac{h^*}{h}}, \qquad (\text{Eq } 1)$$

where H is the nanohardness, h is the indentation depth, H_0 is the material hardness at infinite indentation depth, and h^* is the characteristic length scale. The primary reason for the different tendencies exhibited by the nano- and microhardness is hindrance due to microscale defects,
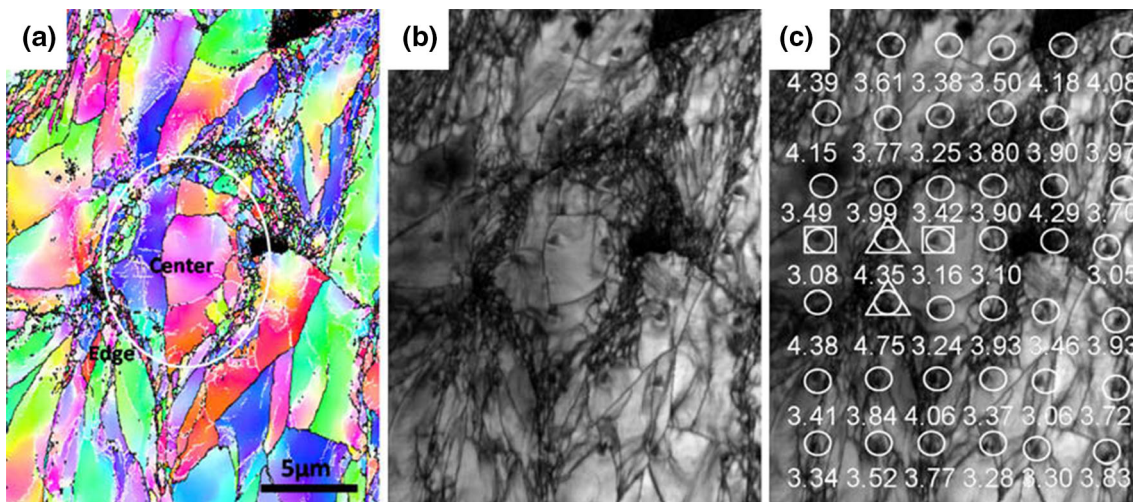

Fig. 28 EBSD characterization of Ni coating after nanoindentation: (a) Euler angle map, (b) image quality (IQ) map, and (c) IQ map with local hardness (Ref 82)

such as pores and debonding of particles. For the nanohardness, the evaluation is almost unaffected by such microscale defects because the measuring range is confined to the nanoscale and is assisted by a low load (1-20 mN). However, evaluation of microhardness cannot be
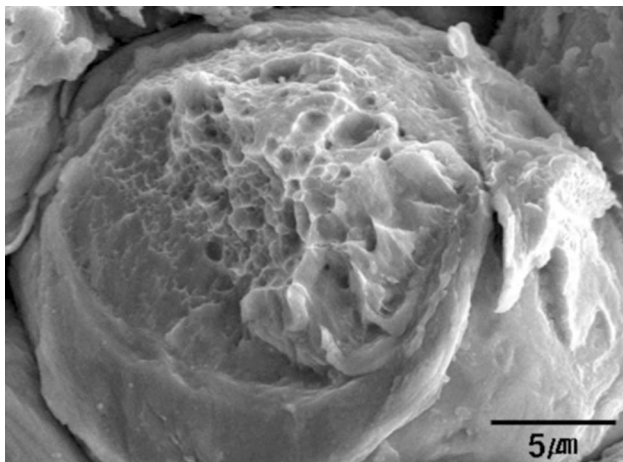

Fig. 29 SEM image of fracture surface in kinetic-sprayed Ti deposit with ductile dimple fracture mode (Ref 76)
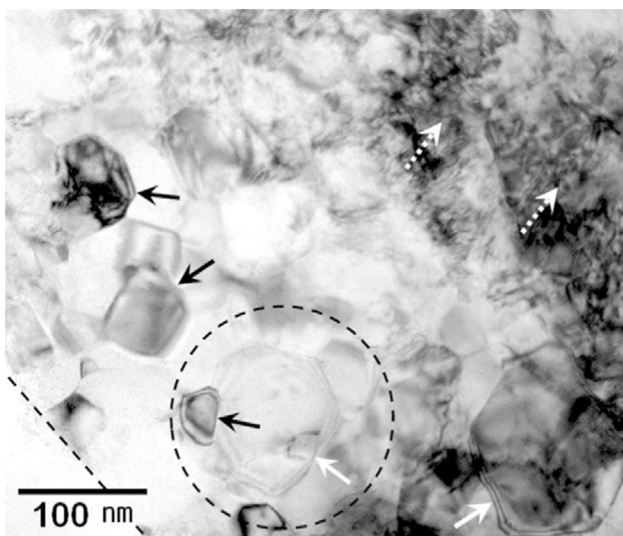

Fig. 30 Highly magnified bright-field TEM image near interparticle boundary of kinetic-sprayed Ni deposit (Ref 52)

free from the influence of microscale defects (i.e., pores, interparticle cracks, and interparticle debonding). Figure 31 shows indents caused by microhardness measurements for bulk Ti and Ti deposits (Ref 111). In the specimen with poor microhardness (Table 3), there is obvious distortion of the indents, which seems to be caused by debonding between particles (Fig. 31c, d). Thus, pores and debonding of particles contributed to the reduction of microhardness. However, as shown in Fig. 31(e, f) and (g, h), the distortion in the Ti deposits was minimized when using enhanced process conditions (increased particle velocity), corresponding to the higher microhardness of the well-formed Ti deposits compared with bulk Ti (Table 3); That is, to achieve a kinetic-sprayed metal deposit of good quality, the bonding quality must be maximized by using optimized process conditions. However, some limited parts of the deposit (i.e., the interface region) usually possess superior properties, regardless of the process conditions.

Furthermore, even for the case of Cu (Ref 12), which is one of the materials easily deposited by kinetic spraying, the tensile strength of the as-sprayed layer (<100 MPa) is much lower than that of cold-rolled plate (~390 MPa). The elongation to failure was also poor for as-sprayed Cu deposits ($<0.1\%$) relative to cold-rolled Cu plate (~2.6%). The reason for such inferior tensile strength and ductility in the kinetic-sprayed specimens can be determined by observing the fracture surface of the cold-rolled and as-sprayed Cu (Fig. 32). As shown in Fig. 32(b), brittle fracture was generated along the interparticle boundary. No dimples appeared on the fracture surface, which is evidence of intimate bonding in the kinetic spray process. Thus, the degradation in the evaluated mechanical properties of the kinetic-sprayed Cu deposit occurred because of weakening caused by imperfect bonding between particles.

However, if optimized process conditions are applied in fabrication of metal deposits via a kinetic spray process, metal coatings with mechanical properties almost equivalent to those of the bulk metal can be formed, although it is impossible to achieve perfect interface bonding throughout the whole layer. Kim et al. (Ref 122) reported that a kinetic-sprayed thick Al deposit showed superior mechanical properties relative to bulk Al fabricated by equal-channel angular pressing, which is a fabrication method involving severe plastic deformation (Ref 168, 169).

Table 3 Mean hardness and splat adhesion strength of kinetic-sprayed Ti deposits under various process conditions, measured by indentation method

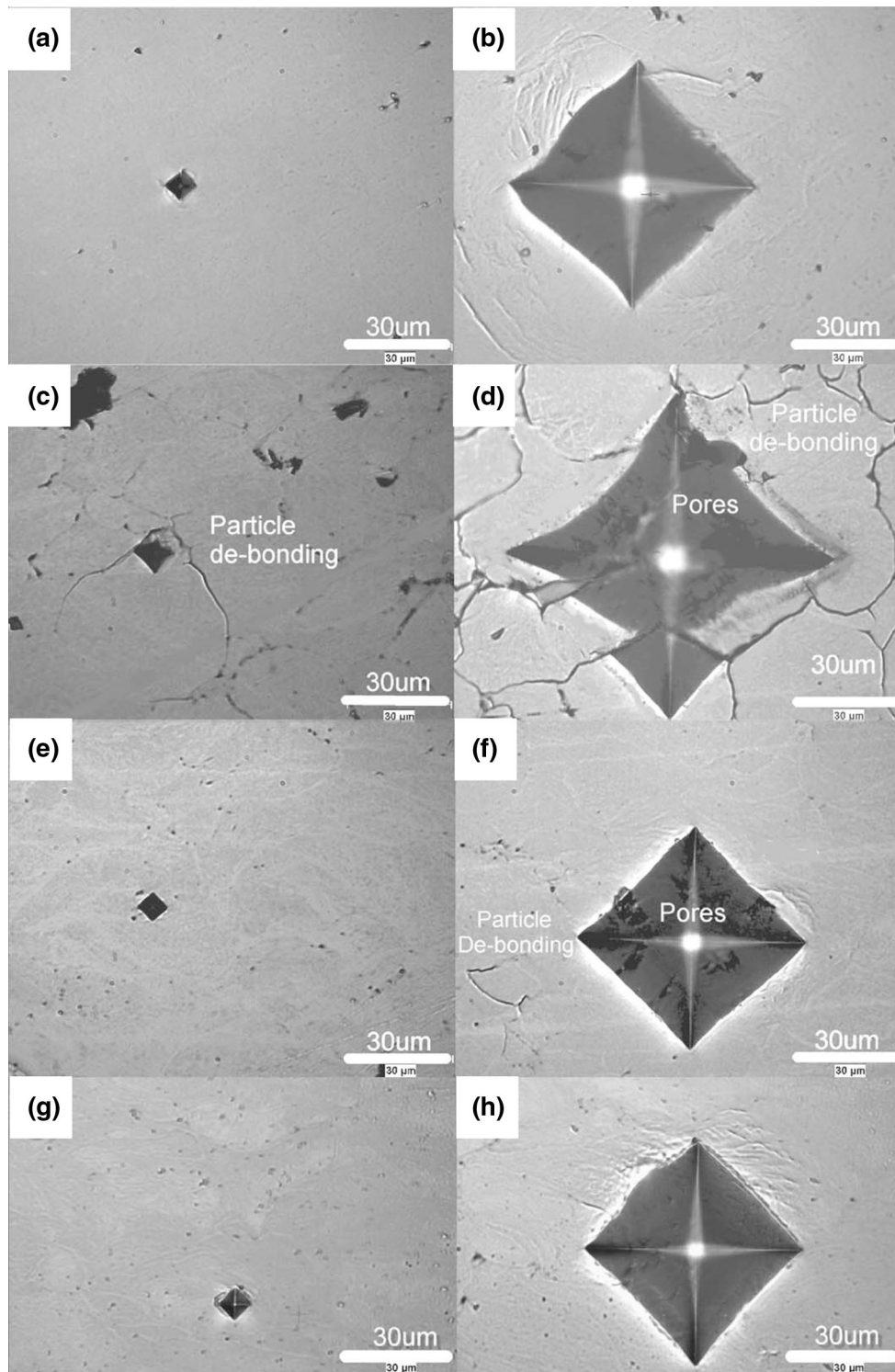|	Nanohardness (GPa)	Microhardness (GPa)	Splat adhesion (MPa)
608 m/s (N$_2$ at 300 °C and 3 MPa)	2.92 ± 0.12	1.14 ± 0.03	32 ± 52
648 m/s (N$_2$ at 500 °C and 3 MPa)	2.86 ± 0.13	1.32 ± 0.09	92 ± 51
688 m/s (N$_2$ at 600 °C and 3 MPa)	3.06 ± 0.07	1.85 ± 0.04	128 ± 86
785 m/s (N$_2$ at 750 °C and 4 MPa)	3.15 ± 0.20	2.21 ± 0.08	152 ± 16
805 m/s (N$_2$ at 800 °C and 4 MPa)	2.98 ± 0.10	2.15 ± 0.35	238 ± 33
1173 m/s (He at 350 °C and 4 MPa)	2.60 ± 0.08	2.57 ± 0.04	254 ± 21
Bulk Ti	2.19 ± 0.04	1.97 ± 0.06	...

Fig. 31 Optical microscopy images of 0.1-N and 5-N indents in: (a, b) bulk Ti plate, and as-sprayed Ti layers deposited with particle velocity of (c, d) 608 m/s, (e, f) 805 m/s, and (g, h) 1173 m/s (Ref 109)
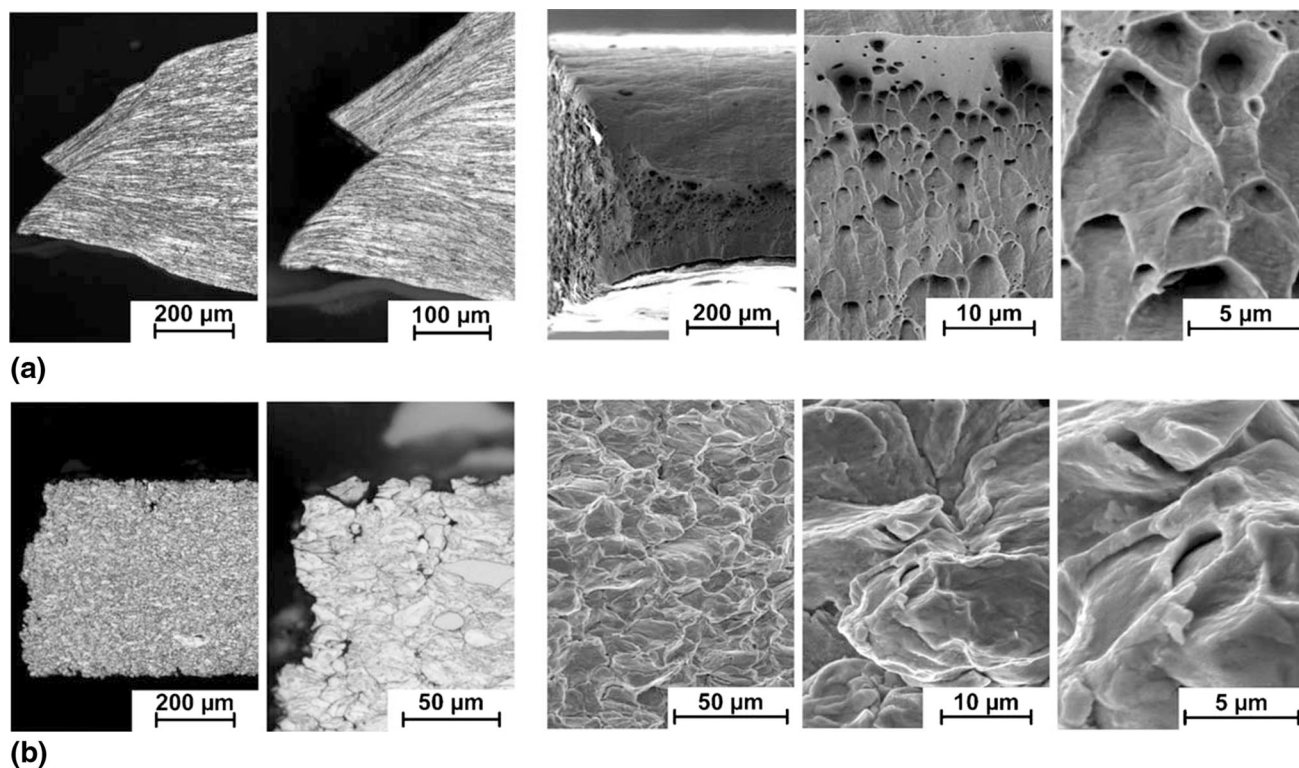
Fig. 32 Microstructure and morphology of fracture surface in (a) cold-rolled Cu plate and (b) as-sprayed Cu deposit fabricated by kinetic spray process (Ref 12)

5. Summary

Throughout this paper, the correlations among impact conditions, interface reactions, microstructural evolution, and mechanical properties have been presented. Although these relationships cannot be systematically classified into specific cases due to their complexity, there are critical factors for each relationship. For interface reactions, the most important factor is the interactions between given impact conditions (i.e., particle velocity, particle and substrate temperatures, relative hardness of particles and substrate, oxidation state, and impact angle) and the material properties. It is possible to predict the interface reactions for given impact conditions using material-specific parameters from the Johnson–Cook plasticity model and the general properties of the metal feedstock powder. The microstructural response of the feedstock material is primarily determined by the interactions between its material properties and the given thermal/stored strain energy. In most cases, nanocrystalline structure is formed along the bonding interface through grain refinement and static/dynamic restoration. Accordingly, the local mechanical properties (i.e., ductility, hardness, and toughness) of the interface region of the coating layer are superior to those of the bulk metal, whereas the microscale properties are usually inferior because of microdefects, such as pores and interparticle debonding, unless optimized process conditions are applied.

References

1. A.P. Alkhimov, A.N. Papyrin, V.F. Kosarev, N.I. Nesterovich, and M.M. Shushpanov, Gas-Dynamic Spray Method for Applying a Coating, US Patent 5,302,414, 12 Apr 1994
2. R.C. Dykhuizen and M.F. Smith, Gas Dynamic Principles of Cold Spray, *J. Therm. Spray Technol.*, 1998, **7**(2), p 205-212
3. V.F. Kosarev, S.V. Klinkov, A.P. Alkhimov, and A.N. Papyrin, On Some Aspects of Gas Dynamics of the Cold Spray Process, *J. Therm. Spray Technol.*, 2003, **12**(2), p 265-281
4. A.P. Alkhimov, V.F. Kosarev, and S.V. Klinkov, The Features of Cold Spray Nozzle Design, *J. Therm. Spray Technol.*, 2001, **10**(2), p 375-381
5. M. Grujicic, C.L. Zhao, C. Tong, W.S. DeRosset, and D. Helfritch, Analysis of the Impact Velocity of Powder Particles in the Cold-Gas Dynamic-Spray Process, *Mater. Sci. Eng. A*, 2004, **368**, p 222-230
6. B. Jodoin, Cold Spray Nozzle Mach Number Limitation, *J. Therm. Spray Technol.*, 2002, **11**(4), p 496-507
7. W.-Y. Li and C.-J. Li, Optimal Design of a Novel Cold Spray Gun Nozzle at a Limited Space, *J. Therm. Spray Technol.*, 2005, **14**(3), p 391-396
8. H.-B. Jung, J.-I. Park, S.-H. Park, H.-J. Kim, C. Lee, and J.-W. Han, Effect of the Expansion Ratio and Length Ratio on a Gas-Particle Flow in a Converging-Diverging Cold Spray Nozzle, *Met. Mater. Int.*, 2009, **15**, p 967-970

9. T. Hussain, D.G. McCartney, P.H. Shipway, and T. Marrocco, Corrosion Behavior of Cold Sprayed Titanium Coatings and Free Standing Deposit, *J. Therm. Spray Technol.*, 2011, **20**(1–2), p 260-274

10. D. Dzhurinskiy, E. Maeva, E. Leshchinsky, and R.G. Maev, Corrosion Protection of Light Alloys Using Low Pressure Cold Spray, *J. Therm. Spray Technol.*, 2012, **21**(2), p 302-313

11. W.B. Choi, L. Li, V. Luzin, R. Neiser, T. Gnaupel-Herold, H.J. Prask, S. Sampath, and A. Gouldstone, Integrated Characterization of Cold Sprayed Aluminum Coatings, *Acta Mater.*, 2007, **55**, p 857-866

12. F. Gartner, T. Stoltenhoff, J. Voyer, H. Kreye, S. Riekehr, and M. Kocak, Mechanical Properties of Cold-Sprayed and Thermally Sprayed Copper Coatings, *Surf. Coat. Technol.*, 2006, **200**, p 6770-6782

13. Y. Tao, T. Xiong, C. Sun, L. Kong, X. Cui, T. Li, and G.-L. Song, Microstructure and Corrosion Performance of a Cold Sprayed Aluminum Coating on AZ91D Magnesium Alloy, *Corros. Sci.*, 2010, **52**, p 3191-3197

14. P. Richer, M. Yandouzi, L. Beauvais, and B. Jodoin, Oxidation Behavior of CoNiCrAlY Bond Coats Produced by Plasma, HVOF and Cold Gas Dynamic Spraying, *Surf. Coat. Technol.*, 2010, **204**, p 3962-3974

15. S.B. Pitchuka, D. Lahiri, G. Sundararajan, and A. Agarwal, Scratch-Induced Deformation Behavior of Cold-Sprayed Aluminum Amorphous/Nanocrystalline Coatings at Multiple Load Scales, *J. Therm. Spray Technol.*, 2014, **23**(3), p 502-513

16. Q. Zhang, C.-J. Li, C.-X. Li, G.-J. Yang, and S.-C. Lui, Study of Oxidation Behavior of Nanostructured NiCrAlY Bond Coatings Deposited by Cold Spraying, *Surf. Coat. Technol.*, 2008, **202**, p 3378-3384

17. H.-J. Kim, C. Lee, and S.-Y. Hwang, Superhard Nano WC-12%Co Coatings by Cold Spray Deposition, *Mater. Sci. Eng. A*, 2005, **391**, p 243-248

18. A. Manap, A. Nakano, and K. Ogawa, The Protectiveness of Thermally Grown Oxides on Cold Sprayed CoNiCrAlY Bond Coat in Thermal Barrier Coating, *J. Therm. Spray Technol.*, 2012, **21**(3–4), p 586-596

19. H. Assadi, F. Gartner, T. Stoltenhoff, and H. Kreye, Bonding Mechanism in Cold Gas Spraying, *Acta Mater.*, 2003, **51**, p 4379-4394

20. T. Schmidt, F. Gartner, H. Assadi, and H. Kreye, Development of Generalized Parameter Window for Cold Spray Deposition, *Acta Mater.*, 2006, **54**, p 729-742

21. G. Bae, Y. Xiong, S. Kumar, K. Kang, and C. Lee, General Aspects of Interface Bonding in Kinetic Sprayed Coatings, *Acta Mater.*, 2008, **56**, p 4858-4868

22. G. Bae, S. Kumar, S. Yoon, K. Kang, H. Na, H. Kim, and C. Lee, Bonding Features and Associated Mechanisms in Kinetic Sprayed Titanium Coatings, *Acta Mater.*, 2009, **57**, p 5654-5666

23. M. Grujicic, C.L. Zhao, W.S. DeRosset, and D. Helfritch, Adiabatic Shear Instability Based Mechanism for Particles/Substrate Bonding in the Cold-Gas Dynamic-Spray Process, *Mater. Des.*, 2004, **25**, p 681-688

24. R.G. Maev and V. Leshchynsky, Air Gas Dynamic Spraying of Powder Mixtures: Theory and Application, *J. Therm. Spray Technol.*, 2006, **15**(2), p 198-205

25. E. Irissou, J.-G. Legoux, A.N. Ryabinin, B. Jodoin, and C. Moreau, Review on Cold Spray Process and Technology: Part I—Intellectual Property, *J. Therm. Spray Technol.*, 2008, **17**(4), p 495-516

26. H. Singh, T.S. Sidhu, and S.B.S. Kalsi, Cold Spray Technology: Future of Coating Deposition Processes, *Frattura ed Integrita Strutturale*, 2012, **22**, p 69-84

27. J. Karthikeyan, Cold Spray Technology: International Status and USA Efforts, ASB Industries, December 2004

28. T. Schmidt, H. Assadi, F. Gartner, H. Richter, T. Stoltenhoff, H. Kreye, and T. Klassen, From Particle Acceleration to Impact and Bonding in Cold Spraying, *J. Therm. Technol.*, 2009, **18**(5–6), p 794-808

29. Y. Xiong, G. Bae, X. Xiong, and C. Lee, The Effects of Successive Impacts and Cold Welds on the Deposition Onset of Cold Spray Coatings, *J. Therm. Spray Technol.*, 2010, **19**(3), p 575-585

30. M. Grujicic, J.R. Saylor, D.E. Beasley, W.S. DeRosset, and D. Helfritch, Computational Analysis of the Interfacial Bonding between Feed-Powder Particles and the Substrate in the Cold-Gas Dynamic-Spray Process, *Appl. Surf. Sci.*, 2003, **219**, p 211-227

31. P.C. King, G. Bae, S.H. Zahiri, M. Jahedi, and C. Lee, An Experimental and Finite Element Study of Cold Spray Copper Impact onto Two Aluminum Substrates, *J. Therm. Spray Technol.*, 2010, **19**(3), p 620-634

32. Y. Xiong, X. Xiong, S. Yoon, G. Bae, and C. Lee, Dependence of Bonding Mechanisms of Cold Sprayed Coatings on Strain-Rate-Induced Non-equilibrium Phase Transformation, *J. Therm. Spray Technol.*, 2011, **20**(4), p 860-865

33. W.-Y. Li, C. Zhang, C.-J. Li, and H. Liao, Modeling Aspects of High Velocity Impact of Particles in Cold Spraying by Explicit Finite Element Analysis, *J. Therm. Spray Technol.*, 2009, **18**(5–6), p 921-933

34. W.-Y. Li, H. Liao, C.-J. Li, G. Li, C. Coddet, and X. Wang, On High Velocity Impact of Micro-sized Metallic Particles in Cold Spraying, *Appl. Surf. Sci.*, 2006, **253**, p 2852-2862

35. W.-Y. Li, C.-J. Li, and G.-J. Yang, Effect of Impact-Induced Melting on Interface Microstructure and Bonding of Cold-Sprayed Zinc Coating, *Appl. Surf. Sci.*, 2010, **257**, p 1516-1523

36. J. Wu, H. Fang, S. Yoon, H.-J. Kim, and C. Lee, The Rebound Phenomenon in Kinetic Spraying Deposition, *Scr. Mater.*, 2006, **54**, p 665-669

37. C.-J. Li, W.-Y. Li, Y.-Y. Wang, G.-J. Yang, and H. Fukanuma, A Theoretical Model for Prediction of Deposition Efficiency in Cold Spraying, *Thin Solid Films*, 2005, **489**, p 79-85

38. T.H. Van Steenkiste, J.R. Smith, and R.E. Teets, Aluminum Coatings via Kinetic Spray with Relatively Large Powder Particles, *Surf. Coat. Technol.*, 2002, **154**, p 237-252

39. R.C. Dykhuizen, M.F. Smith, D.L. Gilmore, R.A. Neiser, X. Jiang, and S. Sampath, Impact of High Velocity Cold Spray Particles, *J. Therm. Spray Technol.*, 1999, **8**(4), p 559-564

40. R. Morgan, P. Fox, J. Pattison, C. Sutcliffe, and W. O'Neill, Analysis of Cold Gas Dynamically Sprayed Aluminum Deposits, *Mater. Lett.*, 2004, **58**, p 1317-1320

41. T. Novoselova, P. Fox, R. Morgan, and W. O'Neill, Experimental Study of Titanium/Aluminum Deposits Produced by Cold Gas Dynamic Spray, *Surf. Coat. Technol.*, 2006, **200**, p 2775-2783

42. M. Fukumoto, M. Mashiko, M. Yamada, and E. Yamaguchi, Deposition Behavior of Copper Fine Particles onto Flat Substrate Surface in Cold Spraying, *J. Therm. Spray Technol.*, 2010, **19**(1–2), p 89-94

43. S.H. Zahiri, C.I. Antonio, and M. Jahedi, Elimination of Porosity in Directly Fabricated Titanium via Cold Gas Dynamic Spraying, *J. Mater. Process. Technol.*, 2009, **209**, p 922-929

44. J. Lee, S. Shin, H.-J. Kim, and C. Lee, Effect of Gas Temperature on Critical Velocity and Deposition Characteristics in Kinetic Spraying, *Appl. Surf. Sci.*, 2007, **253**, p 3512-3520

45. S.H. Zahiri, W. Yang, and M. Jahedi, Characterization of Cold Spray Titanium Supersonic Jet, *J. Therm. Spray Technol.*, 2009, **18**(1), p 110-117

46. C.-J. Li and W.-Y. Li, Deposition Characteristics of Titanium Coating in Cold Spraying, *Surf. Coat. Technol.*, 2003, **167**, p 278-283

47. J. Wu, H. Fang, S. Yoon, H.-J. Kim, and C. Lee, Measurement of Particle Velocity and Characterization of Deposition in Aluminum Alloy Kinetic Spraying Process, *Appl. Surf. Sci.*, 2005, **252**, p 1368-1377

48. S. Shin, S. Yoon, Y. Kim, and C. Lee, Effect of Particle Parameters on the Deposition Characteristics of a Hard/Soft-Particles Composite in Kinetic Spraying, *Surf. Coat. Technol.*, 2006, **201**, p 3457-3461

49. W. Wong, E. Irissou, A.N. Ryabinin, J.-G. Legoux, and S. Yue, Influence of Helium and Nitrogen Gases on the Properties of Cold Gas Dynamic Sprayed Pure Titanium Coatings, *J. Therm. Spray Technol.*, 2011, **20**(1–2), p 213-226

50. P.C. King and M. Jahedi, Relationship Between Particle Size and Deformation in the Cold Spray Process, *Appl. Surf. Sci.*, 2010, **256**, p 1735-1738

51. G. Bae, K. Kang, H. Na, J.-J. Kim, and C. Lee, Effect of Particle Size on the Microstructure and Properties of Kinetic Sprayed Nickel Coatings, *Surf. Coat. Technol.*, 2010, **204**, p 3326-3335

52. G. Bae, J. Jang, and C. Lee, Correlation of Particle Impact Conditions with Bonding, Nanocrystal Formation and Mechanical Properties in Kinetic Sprayed Nickel, *Acta Mater.*, 2012, **60**, p 3524-3535

53. X.-J. Ning, J.-H. Jang, and H.-J. Kim, The Effects of Powder Properties on In-Flight Particle Velocity and Deposition Process During Low Pressure Cold Spray Process, *Appl. Surf. Sci.*, 2007, **253**, p 7449-7455

54. C.-J. Li, H.-T. Wang, Q. Zhang, G.-J. Yang, W.-Y. Li, and H.L. Liao, Influence of Spray Materials and Their Surface Oxidation on the Critical Velocity in Cold Spraying, *J. Therm. Spray Technol.*, 2010, **19**(1–2), p 95-101

55. K. Kang, S. Yoon, Y. Ji, and C. Lee, Oxidation Dependency of Critical Velocity for Aluminum Feedstock Deposition in Kinetic Spraying Process, *Mater. Sci. Eng. A*, 2008, **486**, p 300-307

56. W.-Y. Li, C.-J. Li, and H. Liao, Significant Influence of Particle Surface Oxidation on Deposition Efficiency, Interface Microstructure and Adhesive Strength of Cold-Sprayed Copper Coatings, *Appl. Surf. Sci.*, 2010, **256**, p 4953-4958

57. Y. Ichikawa and K. Ogawa, Effect of Substrate Surface Oxide Film Thickness on Deposition Behavior and Deposition Efficiency in the Cold Spray Process, *J. Therm. Spray Technol.*, 2015, **24**(7), p 1269-1276

58. K. Kim and S. Kuroda, Amorphous Oxide Film Formed by Dynamic Oxidation During Kinetic Spraying of Titanium at High Temperature and Its Role in Subsequent Coating Formation, *Scr. Mater.*, 2010, **634**, p 215-218

59. W.-Y. Li, C. Zhang, X.P. Guo, G. Zhang, H.L. Liao, C.-J. Li, and C. Coddet, Effect of Standoff Distance on Coating Deposition Characteristics in Cold Spraying, *Mater. Des.*, 2008, **29**, p 297-304

60. K. Binder, J. Gottschalk, M. Kollenda, F. Gartner, and T. Klassen, Influence of Impact Angle and Gas Temperature on Mechanical Properties of Titanium Cold Spray Deposits, *J. Therm. Spray Technol.*, 2011, **20**(1–2), p 234-242

61. D.L. Gilmore, R.C. Dykhuizen, R.A. Neiser, T.J. Roemer, and M.F. Smith, Particle Velocity and Deposition Efficiency in the Cold Spray Process, *J. Therm. Spray Technol.*, 1999, **8**(4), p 576-582

62. P. Richer, B. Jodoin, L. Ajdelsztajn, and E.J. Lavernia, Substrate Roughness and Thickness Effects on Cold Spray Nanocrystalline Al-Mg Coatings, *J. Therm. Spray Technol.*, 2006, **15**(2), p 246-254

63. S. Kumar, G. Bae, and C. Lee, Deposition Characteristics of Copper Particles on Roughened Substrates Through Kinetic Spraying, *Appl. Surf. Sci.*, 2009, **255**, p 3472-3479

64. T. Han, Z. Zhao, B.A. Gillispie, and J.R. Smith, Effects of Spray Conditions on Coating Formation by the Kinetic Spray Process, *J. Therm. Spray Technol.*, 2005, **14**(3), p 373-383

65. H. Lee, H. Shin, S. Lee, and K. Ko, Effect of Gas Pressure on Al Coatings by Cold Gas Dynamic Spray, *Mater. Lett.*, 2008, **62**, p 1579-1581

66. T. Stoltenhoff, H. Kreye, and H.J. Richter, An Analysis of the Cold Spray Process and Its Coatings, *J. Therm. Spray Technol.*, 2002, **11**(4), p 542-550

67. Y. Li, X.-F. Wang, S. Yin, and S.-L. Xu, Influence of Particle Initial Temperature on High Velocity Impact Process in Cold Spraying, *Procedia Environ. Sci.*, 2012, **12**, p 298-304

68. K.H. Ko, J.O. Choi, and H. Lee, Pretreatment Effect of Cu Feedstock on Cold-Sprayed Coatings, *J. Mater. Process. Technol.*, 2014, **214**, p 1530-1535

69. S. Yin, X. Wang, W.-Y. Li, H. Liao, and H. Jie, Deformation Behavior of the Oxide Film on the Surface of Cold Sprayed Powder Particle, *Appl. Surf. Sci.*, 2012, **259**, p 294-300

70. X.K. Suo, X.P. Guo, W.-Y. Li, M.P. Planche, and H.L. Liao, Investigation of Deposition Behavior of Cold-Sprayed Magnesium Coating, *J. Therm. Spray Technol.*, 2012, **21**(5), p 831-837

71. L. Ajdelsztajn, B. Jodoin, G.E. Kim, and J.M. Schoenung, Cold Spray Deposition of Nanocrystalline Aluminum Alloys, *Metall. Mater. Trans. A*, 2005, **36A**, p 657-666

72. X.L. Zhou, S.J. Mou, X.K. Wu, and J.S. Zhang, Deposition Behavior of Mixed Binary Metallic Powders in Cold Spraying Process, *Appl. Surf. Sci.*, 2011, **257**, p 10628-10633

73. R.S. Lima, J. Karthikeyan, C.M. Kay, J. Lindemann, and C.C. Berndt, Microstructural Characteristics of Cold-Sprayed Nanostructured WC-Co Coatings, *Thin Solid Films*, 2002, **416**, p 129-135

74. P.C. King, S.H. Zahiri, and M. Jahedi, Microstructural Refinement within a Cold-Sprayed Copper Particle, *Metall. Mater. Trans. A*, 2009, **40A**, p 2115-2123

75. C. Borchers, F. Gartner, T. Stoltenhoff, H. Assadi, and H. Kreye, Microstructural and Macroscopic Properties of Cold Sprayed Copper Coatings, *J. Appl. Phys.*, 2003, **93**, p 10064-10070

76. Q. Wang, N. Birbilis, and M.-X. Zhang, Interfacial Structure Between Particles in an Aluminum Deposit Produced by Cold Spray, *Mater. Lett.*, 2011, **65**, p 1576-1578

77. K. Kang, J. Won, G. Bae, S. Ha, and C. Lee, Interfacial Bonding and Microstructural Evolution of Al in Kinetic Spraying, *J. Mater. Sci.*, 2012, **47**, p 4649-4659

78. G. Bae, K. Kang, J.-J. Kim, and C. Lee, Nanostructure Formation and Its Effects on the Mechanical Properties of Kinetic Sprayed Titanium Coating, *Mater. Sci. Eng. A*, 2010, **527**, p 6313-6319

79. Y. Zou, W. Qin, E. Irissou, J.-G. Legoux, S. Yue, and J.A. Szpunar, Dynamic Recrystallization in the Particle/Particle Interfacial Region of Cold-Sprayed Nickel Coating: Electron Backscatter Diffraction Characterization, *Scr. Mater.*, 2009, **61**, p 899-902

80. D. Rafaja, T. Schucknecht, V. Klemm, A. Paul, and H. Barek, Microstructural Characterization of Titanium Coatings Deposited Using Cold Gas Spraying on Al₂O₃ Substrates, *Surf. Coat. Technol.*, 2009, **203**, p 3206-3213

81. C. Moy, J. Cairnet, G. Ranzi, M. Jahedi, and S.P. Ringer, Investigating the Microstructure and Composition of Cold Gas-Dynamic Spray (CGDS) Ti Powder Deposited on Al 6063 Substrate, *Surf. Coat. Technol.*, 2010, **204**, p 3739-3749

82. Y.Y. Zhang and J.S. Zhang, Recrystallization in the Particles Interfacial Region of the Cold-Sprayed Aluminum Coating: Strain-Induced Boundary Migration, *Mater. Lett.*, 2011, **65**, p 1856-1858

83. C. Borchers, F. Gartner, T. Stoltenhoff, and H. Kreye, Microstructural Bonding Features of Cold Sprayed Face Centered Cubic Metals, *J. Appl. Phys.*, 2004, **96**, p 4288-4292

84. Y. Zou, D. Goldbaum, J.A. Szpunar, and S. Yue, Microstructure and Nanohardness of Cold-Sprayed Coatings: Electron Backscattered Diffraction and Nanoindentation Studies, *Scr. Mater.*, 2010, **62**, p 395-398

85. Y. Xion, K. Kang, G. Bae, S. Yoon, and C. Lee, Dynamic Amorphization and Recrystallization of Metals in Kinetic Spray Process, *Appl. Phys. Lett.*, 2008, **92**, p 194101

86. S. Yoon, G. Bae, Y. Xiong, S. Kumar, K. Kang, J.-J. Kim, and C. Lee, Strain-Enhanced Nanocrystallization of a CuNiTiZr Bulk Metallic Glass Coating by a Kinetic Spraying Process, *Acta Mater.*, 2009, **57**, p 6191-6199

87. S. Guetta, M.H. Berger, F. Borit, V. Guipont, M. Jeandin, M. Boustie, Y. Ichikawa, K. Sakaguchi, and K. Ogawa, Influence of Particle Velocity on Adhesion of Cold-Sprayed Splats, *J. Therm. Spray Technol.*, 2009, **18**, p 331-342

88. H. Lee, S. Lee, and K. Ko, Annealing Effects on the Intermetallic Compound Formation of Cold Sprayed Ni, Al Coatings, *J. Mater. Process. Technol.*, 2009, **209**, p 937-943

89. X.-J. Ning, J.-H. Kim, H.-J. Kim, and C. Lee, Characteristics and Heat Treatment of Cold-Sprayed Al-Sn Binary Alloy Coatings, *Appl. Surf. Sci.*, 2009, **255**, p 3933-3939

90. G.-J. Yang, H.-T. Wang, C.-J. Li, and C.-X. Li, Effect of Annealing on the Microstructure and Erosion Performance of Cold-Sprayed FeAl Intermetallic Coatings, *Surf. Coat. Technol.*, 2011, **205**, p 5502-5509

91. W.-Y. Li, C.-J. Li, and H. Liao, Effect of Annealing Treatment on the Microstructure and Properties of Cold-Sprayed Cu Coating, *J. Therm. Spray Technol.*, 2006, **15**(2), p 206-211

92. H. Bu, M. Yandouzi, C. Ju, and B. Jodoin, Effect of Heat Treatment on the Intermetallic Layer of Cold Sprayed Aluminum Coatings on Magnesium Alloy, *Surf. Coat. Technol.*, 2011, **205**, p 4665-4671

93. W.-Y. Li, C.-J. Li, H. Liao, and C. Coddet, Effect of Heat Treatment on the Microstructure and Microhardness of Cold-Sprayed Tin Bronze Coating, *Appl. Surf. Sci.*, 2007, **253**, p 5967-5971

94. H.-T. Wang, C.-J. Li, G.-J. Yang, and C.-X. Li, Effect of Heat Treatment on the Microstructure and Property of Cold-Sprayed Nanostructured FeAl/Al$_2$O$_3$ Intermetallic Composite Coating, *Vacuum*, 2009, **83**, p 146-152

95. H. Lee, S. Jung, S. Lee, and K. Ko, Fabrication of Cold Sprayed Al-Intermetallic Compounds Coatings by Post Annealing, *Mater. Sci. Eng. A*, 2006, **433**, p 139-143

96. T. Novoselova, S. Celotto, R. Morgan, P. Fox, and W. O'Neill, Formation of TiAl Intermetallics by Heat Treatment of Cold-Sprayed Precursor Deposits, *J. Alloys Compd.*, 2007, **436**, p 69-77

97. K. Spencer and M.-X. Zhang, Heat Treatment of Cold Sprayings to Form Protective Intermetallic Layers, *Scr. Mater.*, 2009, **61**, p 44-47

98. K. Kang, H. Park, G. Bae, and C. Lee, Microstructure and Texture of Al Coating During Kinetic Spraying and Heat Treatment, *J. Mater. Sci.*, 2012, **47**, p 4053-4061

99. P.D. Eason, J.A. Fewkes, S.C. Kennett, T.J. Eden, K. Tello, M.J. Kaufman, and M. Tiryakioglu, On the Characterization of Bulk Copper Produced by Cold Gas Dynamic Spray Processing in as Fabricated and Annealed Conditions, *Mater. Sci. Eng. A*, 2011, **528**, p 8174-8178

100. S.H. Zahiri, D. Fraser, and M. Jahedi, Recrystallization of Cold Spray-Fabricated CP Titanium Structures, *J. Therm. Spray Technol.*, 2009, **18**(1), p 16-22

101. A.C. Hall, D.J. Cook, R.A. Neiser, T.J. Roemer, and D.A. Hirschfeld, The Effect of a Simple Annealing Heat Treatment on the Mechanical Properties of Cold-Sprayed Aluminum, *J. Therm. Spray Technol.*, 2006, **15**(2), p 233-238

102. E. Calla, D.G. McCartney, and P.H. Shipway, Effect of Deposition Conditions on the Properties and Annealing Behavior of Cold-Sprayed Copper, *J. Therm. Spray Technol.*, 2006, **15**, p 255-262

103. N. Bala, H. Singh, and S. Prakash, Accelerated Hot Corrosion Studies of Cold Spray Ni-50Cr Coating on Boiler Steels, *Mater. Des.*, 2010, **31**, p 244-253

104. B.S. Deforce, T.J. Eden, and J.K. Potter, Cold Spray Al-5% Mg Coatings for the Corrosion Protection of Magnesium Alloys, *J. Therm. Spray Technol.*, 2011, **20**(6), p 1352-1358

105. H. Bu, M. Yandouzi, C. Lu, D. MacDonald, and B. Jodoin, Cold Spray Blended Al + Mg17Al12 Coating for Corrosion Protection of AZ91D Magnesium Alloy, *Surf. Coat. Technol.*, 2012, **207**, p 155-162

106. H. Koivuluoto, G. Bolelli, L. Lusvarghi, F. Casadei, and P. Vuoristo, Corrosion Resistance of Cold-Sprayed Ta Coatings in Very Aggressive Conditions, *Surf. Coat. Technol.*, 2010, **205**, p 1103-1107

107. N.M. Chavan, B. Kiran, A. Jyothirmayi, P.S. Phani, and G. Sundararajan, The Corrosion Behavior of Cold Sprayed Zinc Coatings on Mild Steel Substrate, *J. Therm. Spray Technol.*, 2013, **22**(4), p 463-470

108. H. Koivuluoto, J. Nakki, and P. Vuoristo, Corrosion Properties of Cold-Sprayed Tantalum Coatings, *J. Therm. Spray Technol.*, 2009, **18**(1), p 75-82

109. H. Koivuluoto, A. Milanti, G. Bolelli, L. Lusvarghi, and P. Vuoristo, High-Pressure Cold-Sprayed Ni and Ni-Cu Coatings: Improved Structures and Corrosion Properties, *J. Therm. Spray Technol.*, 2014, **23**(1–2), p 98-103

110. N. Bala, H. Singh, and S. Prakash, High Temperature Corrosion Behavior of Cold Spray Ni-20Cr Coating on Boiler Steel in Molten Salt Environment at 900 °C, *J. Therm. Spray Technol.*, 2010, **19**(1–2), p 110-118

111. D. Goldbaum, J. Ajaja, R.R. Chromik, W. Wong, S. Yue, E. Irissou, and J.-G. Legoux, Mechanical Behavior of Ti Cold Spray Coatings Determined by a Multi-scale Indentation Method, *Mater Sci. Eng. A*, 2011, **530**, p 253-265

112. J. Ajaja, D. Goldbaum, and R.R. Chromik, Characterization of Ti Cold Spray Coatings by Indentation Methods, *Acta Astronaut.*, 2011, **69**, p 923-928

113. S.M. Kalkhoran, W.B. Choi, and A. Gouldstone, Estimation of Plastic Anisotropy in Ni-5% Al Coatings via Spherical Indentation, *Acta Mater.*, 2012, **60**, p 803-810

114. D. Goldbaum, R.R. Chromik, S. Yue, E. Irissou, and J.-G. Legoux, Mechanical Property Mapping of Cold Sprayed Ti Splats and Coatings, *J. Therm. Spray Technol.*, 2011, **20**(3), p 486-496

115. G. Bolelli, B. Bonferroni, H. Koivuluoto, L. Lusvarghi, and P. Vuoristo, Depth-Sensing Indentation for Assessing the Mechanical Properties of Cold-Sprayed Ta, *Surf. Coat. Technol.*, 2010, **205**, p 2009-2217

116. W.-Y. Li, C. Huang, M. Yu, and H. Liao, Investigation on Mechanical Property of Annealed Copper Particles and Cold Sprayed Copper Coating by a Micro-indentation Testing, *Mater. Des.*, 2013, **46**, p 219-226

117. C.W. Ziemian, M.M. Sharma, B.D. Bouffard, T. Nissley, and T.J. Eden, Effect of Substrate Surface Roughening and Cold Spray Coating on the Fatigue Life of AA2024 Specimens, *Mater. Des.*, 2014, **54**, p 212-221

118. V. Luzin, K. Spencer, and M.-X. Zhang, Residual Stress and Thermo-mechanical Properties of Cold Spray Metal Coatings, *Acta Mater.*, 2011, **59**, p 1259-1270

119. K. Spencer, V. Luzin, N. Matthews, and M.-X. Zhang, Residual Stresses in Cold Spray Al Coatings: the Effect of Alloying and of Process Parameters, *Surf. Coat. Technol.*, 2012, **206**, p 4249-4255

120. R. Ghelichi, D. MacDonald, S. Bagherifard, H. Jahed, M. Guagliano, and B. Jodoin, Microstructure and Fatigue Behavior of Cold Spray Coated Al5052, *Acta Mater.*, 2012, **60**, p 6555-6561

121. J. Wu, J. Yang, H. Fang, S. Yoon, and C. Lee, The Bond Strength of Al–Si Coating on Mild Steel by Kinetic Spraying Deposition, *Appl. Surf. Sci.*, 2006, **252**, p 7809-7814

122. K.-S. Kim, J.-S. Yu, J. Won, C. Lee, S.-J. Kim, S. Lee, and K.-A. Lee, Manufacturing and Compressive Deformation Behavior of High-Strength Aluminum Coating Material Fabricated by Kinetic Spray Process, *Metall. Mater. Trans. A*, 2013, **44A**, p 4876-4879

123. X. Suo, X. Guo, W.-Y. Li, M.-P. Planche, R. Bolot, H. Liao, and C. Coddet, Preparation and Characterization of Magnesium Coating Deposited by Cold Spraying, *J. Mater. Process. Technol.*, 2012, **212**, p 100-105

124. S.V. Raj, R. Pawlik, and W. Loewenthal, Young's Moduli of Cold and Vacuum Plasma Sprayed Metallic Coatings, *Mater. Sci. Eng. A*, 2009, **513–514**, p 59-63

125. D. Goldbaum, J.M. Shockley, R.R. Chromik, A. Rezaeian, S. Yue, J.-G. Legoux, and E. Irissou, The Effect of Deposition Conditions on Adhesion Strength of Ti and Ti6Al4 V Cold Spray Splats, *J. Therm. Spray Technol.*, 2012, **21**(2), p 288-303

126. L. Ajdelsztajn, B. Jodoin, and J.M. Schoenung, Synthesis and Mechanical Properties of Nanocrystalline Ni Coatings Produced by Cold Gas Dynamic Spraying, *Surf. Coat. Technol.*, 2006, **201**, p 1166-1172

127. S. Yoon, C. Lee, and H. Choi, Evaluation of the Effects of the Crystallinity of Kinetically Sprayed Ni-Ti-Zr-Si-Sn Bulk Metallic Glass on the Scratch Response, *Mater. Sci. Eng. A*, 2007, **449–451**, p 285-289

128. J.H. Choi, C. Lee, and D.B. Lee, Oxidation Behavior of Bulk Amorphous Ni$_{57}$Ti$_{18}$Zr$_{20}$Si$_3$Sn$_2$ Coatings Between 473 and 973 K in Air, *J. Alloys Compd.*, 2008, **449**, p 384-388

129. N. Bala, H. Singh, and S. Prakash, Characterization and High-Temperature Oxidation Behavior of Cold-Sprayed Ni-20Cr and Ni-50Cr Coatings on Boiler Steels, *Metall. Mater. Trans. A*, 2011, **42A**, p 3399-3416

130. N. Bala, H. Singh, and S. Prakash, High-Temperature Oxidation Studies of Cold-Sprayed Ni-20Cr and Ni-50Cr Coatings on SAE 213-T22 Boiler Steel, *Appl. Surf. Sci.*, 2009, **255**, p 6862-6869

131. S.V. Raj, C. Barrett, J. Karthikeyan, and R. Garlick, Comparison of the Cyclic Oxidation Behavior of Cold Sprayed CuCrAl-

Coated and Uncoated GRCop-84 Substrates for Space Launch Vehicles, *Surf. Coat. Technol.*, 2007, **201**, p 7222-7234

132. M. Yu, W.-Y. Li, C. Zhang, and H. Liao, Effect of Vacuum Heat Treatment on Tensile Strength and Fracture Performance of Cold-Sprayed Cu-4Cr-2Nb Coatings, *Appl. Surf. Sci.*, 2011, **257**, p 5972-5976

133. T. Marrocco, T. Hussain, D.G. McCartney, and P.H. Shipway, Corrosion Performance of Laser Posttreated Cold Sprayed Titanium Coatings, *J. Therm. Spray Technol.*, 2011, **20**(4), p 909-917

134. Y.H. Yoo, S.H. Lee, J.G. Kim, J.S. Kim, and C. Lee, Effect of Heat Treatment on the Corrosion Resistance of Ni-Based and Cu-Based Amorphous Alloy Coatings, *J. Alloys Compd.*, 2008, **461**, p 304-311

135. B. Al-Magnour, R. Dallala, F. Zhim, R. Mongrain, and S. Yue, Fatigue Behavior of Annealed Cold Sprayed 316L Stainless Steel Coating for Biomedical Applications, *Mater. Lett.*, 2013, **91**, p 352-355

136. N.M. Chavan, M. Ramakrishna, P.S. Phani, D.S. Rao, and G. Sundararajan, The Influence of Process Parameters and Heat Treatment on the Properties of Cold Sprayed Silver Coatings, *Surf. Coat. Technol.*, 2011, **205**, p 4798-4807

137. H. Choi, H. Jo, K. An, S. Yoon, and C. Lee, Tribological Behavior of the Kinetic Sprayed $Ni_{59}Ti_{16}Zr_{20}Si_2Sn_3$ Bulk Metallic Glass, *J. Alloys Compd.*, 2007, **434--435**, p 64-67

138. X. Guo, G. Zhang, W.-Y. Li, Y. Gao, H. Liao, and C. Coddet, Investigation of the Microstructure and Tribological Behavior of Cold-Sprayed Tin-Bronze-Based Composite Coatings, *Appl. Surf. Sci.*, 2009, **255**, p 3822-3828

139. H. Attia, M. Meshreki, A. Korashy, V. Thomson, and V. Chung, Fretting Wear Characteristics of Cold Gas-Dynamic Sprayed Aluminum Alloys, *Tribol. Int.*, 2011, **44**, p 1407-1416

140. C.H. Hager, Jr., J. Sanders, S. Sharma, A. Voevodin, and A. Segall, The Effect of Temperature on Gross Slip Fretting Wear of Cold-Sprayed Nickel Coatings on Ti6Al4V Interfaces, *Tribol. Int.*, 2009, **42**, p 491-502

141. S. Yoon, J. Kim, G. Bae, B. Kim, and C. Lee, Formation of Coating and Tribological Behavior of Kinetic Sprayed Fe-Based Bulk Metallic Glass, *J. Alloys Compd.*, 2011, **509**, p 347-353

142. J. Pattison, S. Celotto, R. Morgan, M. Bray, and W. O'Neill, Cold Gas Dynamic Manufacturing: a Non-thermal Approach to Freeform Fabrication, *Int. J. Mach. Tools Manuf.*, 2007, **47**, p 627-634

143. S. Cadney, M. Brochu, P. Richer, and B. Jodoin, Cold Gas Dynamic Spraying as a Method for Freeforming and Joining Materials, *Surf. Coat. Technol.*, 2008, **202**, p 2801-2806

144. M.E. Lynch, W. Gu, T. El-Wardany, A. Hsu, D. Viens, A. Nardi, and M. Klecka, Design and Topology/Shape Structural Optimisation for Additively Manufactured Cold Sprayed Components, *Virtual Phys. Prototyp.*, 2013, **8**(3), p 213-231

145. Y. Cormier, P. Dupuis, B. Jodoin, and A. Corbeil, Mechanical Properties of Cold Gas Dynamic-Sprayed Near-Net-Shaped Fin Arrays, *J. Therm. Spray Technol.*, 2015, **24**(3), p 476-488

146. A. Sova, S. Grigoriev, A. Okunkova, and I. Smurov, Potential of Cold Gas Dynamic Spray as Additive Manufacturing Technology, *Int. J. Adv. Manuf. Technol.*, 2013, **69**, p 2269-2278

147. S.C. Tjong and H. Chen, Nanocrystalline Materials and Coatings, *Mater. Sci. Eng. R*, 2004, **45**(1–2), p 1-88

148. S. Veprek and S. Reiprich, A Concept for the Design of Novel Superhard Coatings, *Thin Solid Film*, 1995, **286**(1–2), p 64-71

149. G.R. Johnson, and W.H. Cook, A Constitutive Model and Data for Metals Subjected to Large Strains, High Strain Rates and High Temperatures, *Proceedings of the 7th International Symposium on Ballistics*, 1983, p. 541-547

150. MataWeb. Available from: www.matweb.com

151. C. Lee and J. Kim, Microstructure of Kinetic Spray Coatings: a Review, *J. Therm. Spray Technol.*, 2015, **24**(4), p 592-610

152. X.-T. Luo, C.-X. Li, F.-J. Shang, G.-J. Yang, Y.-Y. Wang, and C.-J. Li, High Velocity Impact Induced Microstructure Evolution During Deposition of Cold Spray Coatings: a Review, *Surf. Coat. Technol.*, 2014, **254**, p 11-20

153. E. Nes, Modelling of Work Hardening and Stress Saturation in FCC Metals, *Prog. Mater. Sci.*, 1998, **41**, p 129-193

154. E. Nes, T. Pettersen, and K. Marthinsen, On the Mechanisms of Work Hardening and Flow-Stress Saturation, *Scr. Mater.*, 2000, **43**, p 55-62

155. E. Nes and K. Marthinsen, Modeling the Evolution in Microstructure and Properties During Plastic Deformation of F.C.C.-Metals and Alloys—an Approach Towards a Unified Model, *Mater. Sci. Eng. A*, 2002, **322**, p 176-193

156. E. Nes, K. Marthinsen, and Y. Brechet, On the Mechanisms of Dynamic Recovery, *Scr. Mater.*, 2002, **47**, p 607-611

157. L.E. Murr, K.P. Staudhammer, and M.A. Meyers, *Metallurgical Applications of Shock-Wave and High-Strain-Rate Phenomena*, Elsevier, Amsterdam, 1995

158. C. Borchers, F. Gartner, T. Stoltenhoff, and H. Kreye, Formation of Persistent Dislocation Loops by Ultra-high Strain-Rate Deformation During Cold Spraying, *Acta Mater.*, 2005, **53**, p 2991-3000

159. H. Koivuluoto, M. Honkanen, and P. Vuoristo, Cold-Sprayed Copper and Tantalum Coatings—Detailed FESEM and TEM analysis, *Surf. Coat. Technol.*, 2010, **204**, p 2353-2361

160. G. Bae, K. Kang, and C. Lee, Nanoscale Deformation Twinning at Ultrahigh Strain Rates During Kinetic Spraying of Nickel, *Mater. Lett.*, 2012, **89**, p 320-323

161. L.E. Murr and D. Kuhlmann-Wilsdorf, Experimental and Theoretical Observations on the Relationship Between Dislocation Cell Size, Dislocation Density, Residual Hardness, Peak Pressure and Pulse Duration in Shock-Loaded Nickel, *Acta Metall.*, 1978, **26**, p 847-857

162. C.D. Gu, J.S. Lian, Q. Jiang, and W.T. Zheng, Experimental and Modelling Investigations on Strain Rate Sensitivity of an Electrodeposited 20 nm Grain Sized Ni, *J. Phys. D Appl. Phys.*, 2007, **40**, p 7440-7446

163. C.D. Gu, Y.H. You, Y.L. Yu, S.X. Qu, and J.P. Tu, Microstructure, Nanoindentation, and Electrochemical Properties of the Nanocrystalline Nickel Film Electrodeposited from Choline Chloride-Ethylene Glycol, *Surf. Coat. Technol.*, 2011, **205**, p 4928-4933

164. M.A. Meyers, A. Mishra, and D.J. Benson, The Deformation Physics of Nanocrystalline Metals: Experiments, Analysis, and Computations, *JOM*, 2006, **58**, p 41-48

165. G. Dirras, J. Gubicza, S. Ramtani, Q.H. Bui, and T. Szilagyi, Microstructure and Mechanical Characteristics of Bulk Polycrystalline Ni Consolidated from Blends of Powders with Different Particle Size, *Mater. Sci. Eng. A*, 2010, **527**, p 1206-1214

166. X. Zhang, H. Wang, R.O. Scattergood, J. Narayan, C.C. Koch, A.V. Sergueeva, and A.K. Mukherjee, Studies of Deformation Mechanisms in Ultra-fine-grained and Nanostructured Zn, *Acta Mater.*, 2002, **50**, p 4823-4830

167. X. Shen, J. Lian, Z. Jiang, and Q. Jiang, High Strength and High Ductility of Electrodeposited Nanocrystalline Ni with a Broad Grain Size Distribution, *Mater. Sci. Eng. A*, 2008, **487**, p 410-416

168. C.Y. Yu, P.L. Sun, P.W. Kao, and C.P. Chang, Mechanical Properties of Submicron-Grained Aluminum, *Scr. Mater.*, 2005, **52**, p 359-363

169. M. Kawasaki, Z. Horita, and T.G. Langdon, Microstructural Evolution in High Purity Aluminum Processed by ECAP, *Mater. Sci. Eng. A*, 2009, **524**, p 143-150